FINAL REPORT

Processing for Clutter Evasion in UXO Discrimination

SERDP Project MM-1590

MARCH 2008

Kevin O'Neill
US Army Corps of Engineers - ERDC

Approved for public release;
Distribution is unlimited

SERDP

DoD EPA DOE

Strategic Environmental Research and
Development Program

REPORT DOCUMENTATION PAGE

1. REPORT DATE *(DD-MM-YYYY)*	2. REPORT TYPE	3. DATES COVERED *(From - To)*
13-03-2008	Final Technical Report	03-01-2007 to 31-01-2008

4. TITLE AND SUBTITLE

Processing for Clutter Evasion in UXO Discrimination

5a. CONTRACT NUMBER

5b. GRANT NUMBER

5c. PROGRAM ELEMENT NUMBER

6. AUTHOR(S)

Kevin O'Neill

5d. PROJECT NUMBER

MM-1590

5e. TASK NUMBER

5f. WORK UNIT NUMBER

7. PERFORMING ORGANIZATION NAME(S) AND ADDRESS(ES)

U.S. Army Corps of Engineers, Engineer Research and Development Center

8. PERFORMING ORGANIZATION REPORT NUMBER

9. SPONSORING/MONITORING AGENCY NAME(S) AND ADDRESS(ES)

DoD Strategic Environmental Research and Development Program
901 North Stuart Street, Suite 303
Arlington, VA 22203
Phone: (703) 696-2117

10. SPONSOR/MONITOR'S ACRONYM(S)

11. SPONSOR/MONITOR'S REPORT NUMBER(S)

12. DISTRIBUTION/AVAILABILITY STATEMENT

Unlimited

13. SUPPLEMENTARY NOTES

14. ABSTRACT

Innovative signal processing techniques, derived from basic physics, were applied to electromagnetic induction data to enhance its suitability for UXO discrimination processing. In all simulations and field tests, upward continuation (UC) of surface data succeeded in suppressing clutter signals relative to those from deeper UXOs. This was the case even when the clutter signal was two to three times the strength of the broader UXO response in which it was embedded. Downward continuation (DCN) for the purposes of focusing on subsurface source locations is inherently more problematical, and is only recommended with caution. Ill-conditioning and attendant amplification of signal noise tends to plague DCN, and is likely to occur to some degree even in UC. Methods were identified and developed for analyzing and controlling such ill-conditioning reliably by spectral truncation. The predictive methods here require no particular target models, no optimizations, and no searches for target location, orientation, and properties. Altogether, the results of the project form the basis for development of simple and fast "model-free" discrimination algorithms.

15. SUBJECT TERMS

Unexploded ordnance, UXO, clutter, environmental cleanup, electromagnetic induction, ground penetrating radar

16. SECURITY CLASSIFICATION OF:			17. LIMITATION OF ABSTRACT	18. NUMBER OF PAGES	19a. NAME OF RESPONSIBLE PERSON
a. REPORT	b. ABSTRACT	c. THIS PAGE	UU		Kevin O'Neill
U	U	U			19b. TELEPHONE NUMBER *(Include area code)* 603-646-4312

Reset

ACKNOWLEDGMENTS

ACRONYMS & ABBREVIATIONS

APG: Aberdeen Proving Ground

Co-PI: Co-principal investigator

DCN: Downward continuation

EMI: Electromagnetic Induction

FD: Frequency domain

[I]FFT: [Inverse] Fast Fourier Transform

FT: Frequency truncation

GPS: Global positioning system

NSMC : Normalized Surface Magnetic Charge formulation

PI: Principal Investigator

Rx: Receiver

SERDP: DoD Strategic Environmental Research and Development Program

SNR: Signal to noise ratio

TD: Time domain

Tx: Transmitter

UC: Upward continuation

UXO: Unexploded ordnance

TABLE OF CONTENTS

LIST OF FIGURES

1. Introduction, Summary, and Recommendations

The objective of this project was to explore ways to process magnetometer or electromagnetic induction (EMI) sensor data so that UXO discrimination processing UXO can be enhanced. Suppression of clutter was a principal focus. To this end, magnetic field data obtained above and near the ground surface was regarded as something of a boundary condition. As such, it should allow inference of magnetic fields or associated source distributions either upwards or downwards. The former is done to reduce noise and clutter signals, the latter to observe concentration of field or source values around the location of a subsurface object of interest. This was done here solely on the basis of the governing physics, without application of any particular kind of target modeling and its attendant optimization searches for position, orientation, and target properties. Classical geophysical processing of this sort, using the data over a measurement surface from a single, widespread response field, constitutes "continuation" of that field. To our knowledge, this study is the first attempt to apply the concepts to transient electromagnetic induction surveying, particularly for the kind of high-resolution, shallow sensing needed for UXO discrimination. Our application in EMI is distinguished by the fact that oblique (non-vertical) magnetic field components must be used, and the associated source distributions computed must be displaced from the plane of measurement.

For true continuation, it is essential that the measurements all pertain to a single, though spatially varying field. In magnetometry surveying, the excitation (primary) field is the earth's magnetic field. For all practical purposes, this static field is uniform over the survey area around a target. All measured responses therefore constitute static responses to the same excitation. In particular, all data obtained around a buried object simply constitute samples at different locations of the same response field emanating from the target, as that field varies in magnitude and vector orientation from place to place. The time domain (TD) EMI system used in this project is similar in its nature, despite the transience in the responses. Here the transmitted primary field, while different from the earth's field, is also unchanging in magnitude and orientation over the region around the target. While surveyors rove about with local receivers, the excitation of the target is always the same; its internal response is always the same; and it is always producing the same, spatially varying exterior distribution of magnetic field in response, which is observed from different vantage points. As the TD EMI data obtained here constitute a distributed sampling of

the same, single response field it can likewise serve as a consistent boundary condition, or the equivalent, for that field. The receivers used here are magnetometers of much the same kind as are used in static magnetometry surveys. At each point in time they simply catch a snapshot of the transient magnetic field. All results developed here for TD EMI thus apply directly to treatment of magnetometry data.

Note that the nature of the data described above is fundamentally different from that obtained with most of the popular man- or cart-portable EMI sensors used in UXO surveying and related studies (EM-61, EM-63, GEM sensors...).   Those sensors are "mono-static" in the sense that local transmitters and receivers are approximately co-located. As a sensor of this sort proceeds through a survey, the spatial relation between the transmitter and target constantly changes. The primary field impinging on the target constantly changes. Data obtained at each location is a sample only of the field in response to the excitation transmitted from that location. Therefore a spatial array of such data cannot constitute a boundary condition, or the equivalent, in the same sense as used above. One might say that data at different points constitute samples of different boundary conditions, i.e. from a different fields. Consequently the data cannot be used for continuation, at least in the classical sense. We return to the topic of upward or downward projection of data from mono-static sensors in our recommendations below. Meanwhile, all work in this project pertains to more classical continuation of single fields.

To our knowledge, in connection with surveying applicable to UXO discrimination only some short distance upward continuation of static magnetometry data has been applied heretofore [1]. The classic 1965 text by Grant and West [2] still provides an excellent treatment of the fundamental relations needed, as well as some vital computational maneuvers, if only discussed with reference to static magnetic and gravitational fields. In those areas of application, the possible utility of upward and, occasionally, downward continuation are recognized in well known contemporary geophysics texts, e.g. [3, 4]

Clutter is the bane of EMI surveying for subsurface UXOs under realistic circumstances. Isolating the contributions of different signal sources and suppressing clutter responses would take us a long way towards reliable subsurface UXO discrimination. The work performed here successfully suppressed clutter in field data, even when the local clutter signal was two to three times that of the broader underlying UXO response and was situated directly on and within it. The success of the approach is directly tied to the fact that it relies on the governing physics [5,

6], and not on signal processing stratagems divorced from that physics or idealizing it unduly. Beyond use of the applicable physics in the numerical formulations and computations, that physics is also at the root of the phenomenology exploited for advantage in upward continuation. The relevant phenomenology is explained briefly as follows.

Consider the response from a discrete object that is subject always to the same primary field, when the receiver is at least a characteristic length from the object. The magnitude of the signal is (approximately) inversely proportional to the cube of the distance d between receiver and object,

$$S \sim \frac{b}{d^3} \tag{1}$$

where the constant of proportionality a depends partly on shape and object composition but most significantly on the size of the object. For example, in the case of a sphere, b is proportional to the object's volume. Thus a sphere with a diameter that is substantially larger than that of another will produce a larger signal in proportion to the cube of the ratio of their diameters, if other things are equal. We assume here that, from the point of view of UXO clean up, to qualify as a clutter item an object must be significantly smaller than a target of interest, i.e. UXO. So, why would one worry about an inherently smaller signal? The answer is that "other things are [not!] equal." By (1), a small metallic item on the ground surface that is, say, ten times closer to a sensor than a buried UXO gains in relative signal magnitude by a factor of 10^3, relative to what would be seen if they were the same distance away. This can often more than make up for the inherent weakness of the clutter's response, raising it to problematical prominence. Overall, clutter will only be important if it is near the surface.

Upward continuation can be used to take advantage of this kind of power law signal dependence to suppress the relative importance of near-surface clutter. From the discussion above, if the magnitudes of two signals from a given object are compared, when obtained from different distances d_1 and d_2, the ratio of signal strengths will be

$$\frac{S_2}{S_1} \sim \left(\frac{d_1}{d_2} \right)^3 \tag{2}$$

Thus raising the observation point relative to a near-surface piece of clutter will engender a much larger proportional diminution of signal strength than would be the case for a deeper target of interest. See Figure 1. As the sensor is raised, the quantity $(dc_1/dc_2)^3$ diminishes the clutter's response by a much greater amount than $(dt_1/dt_2)^3$ reduces the UXO's.
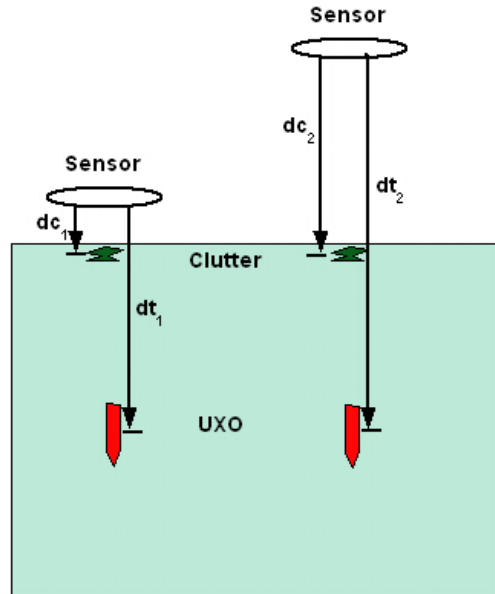
Figure 1. Two elevations of a sensor (receiver) relative to a combination of near-surface clutter item and deeper UXO.

This effect was explored in some detail by the PI in another SERDP project (MM-1282) and was reported in its Final Technical Report as well as reference [7]. As noted in those references, the principal difficulty in trying to take advantage of this phenomenon is that it may be impractical to raise the sensor. It may be physically quite difficult to do so, and perhaps more fundamentally, all the signals involved may become too weak to be useful. Basically, in trying to shift the relative balance of target and clutter signals one may produce overall SNRs that are intolerable. The motivation for pursuing upward continuation (UC) comes specifically from the recognition that it will not be troubled by these problems. We do not have to worry about generating worse relative noise levels at greater distances if we do not actually have to perform the measurements. More specifically, UC will actually tend to *increase* the SNR relative to random noise and error. Just as UC will reduce the kind of signal perturbation caused by clutter such as that indicated schematically in Figure 1, it will also reduce irregularities caused by other

perturbations such as uneven ground effects, positional errors, etc. Both simulations (Section 3.1) and field tests (Section 3.2) demonstrate this, while Section 5 explores some of the basis for it.

Downward continuation (DCN) has various meanings in the geophysics literature, sometimes phasing into broader inferences of subsurface structures and phenomena than just computation of signals at lower (subsurface) elevations. In any case, its purpose is generally to isolate subsurface sources for signals of interest. Here, UC was accomplished by solving for a distribution of equivalent magnetic sources over some plane at an arbitrary distance below that on which data were obtained. These sources can then predict the signal that would be obtained at any location above the original data plane. This is a much simpler computational approach than those in noise-amplifying differential equation UC approaches. Our UC system goes through the same computational motions as would be required to solve for sources over deeper and deeper planes, as in a variety of DCN. The same overall algorithms were used here for both UC and (what we are calling) downwards continuation.

Solution for sources over a plane displaced from the data plane brings ill-conditioning issues to the fore, for reasons explained in Section 5. The deeper the source plane, the worse the ill-conditioning, until a very modest amount of noise or clutter in data causes completely unacceptable distortions in the computations. We show here that this ill-conditioning is completely controllable by means of the spectral truncation methods. Two methods are investigated, namely, 1) Fourier transformation of both data and source distributions into the spatial (not electromagnetic) frequency domain, with truncation of higher and/or weaker frequency content; and 2) transformation into an eigen-system framework and truncation of equations with weak eigenvalues. The gist of each of these approaches is to translate the problem into a basis in which each degree of freedom (coefficient) has a distinctly independent influence on the system, and weak participants are readily recognized and discarded. The results suggest that, while both methods stabilize the solution impressively in the face of enormous condition numbers, neither is likely to be very useful for focusing on subsurface source locations. The spectral truncation necessary for stabilization limits the resolution of the computations. At the same time, the frequency truncation (FT) approach appears superior in consistency and reliability, which relates to the nature of the integral operators used. Examples suggest that FT may also be able to suppress amplification of equivalent sources associated with clutter items more shallow than the plane of equivalent sources. This strong clutter amplification effect, which compounds

but is different from noise amplification by ill-conditioning, is in itself enough to recommend caution, if not complete distaste for DCN.

Conclusions together with recommendations for follow-on work are as follows:

1. **Downward continuation (DCN) appears to have limited appeal**, even if the daunting problems of ill-conditioning and clutter amplification are dealt with successfully. Spatial **frequency truncation (FT) appears capable of stabilizing DCN** calculations while suppressing clutter amplification. FT **warrants further investigation**, particularly because some of the same problems appear in the generally more appealing upward continuation (UC) computations.

2. **Upward continuation was eminently successful at clutter and noise suppression in all simulation and field examples considered**. While ill-conditioning issues can arise even in UC calculations, they appear to be readily controlled by spectral truncation of the data and of the inferred source distributions. Data were continued easily up to elevations where signals were dominated by a deeper UXO, even when very strong signals from near-surface clutter items were present in the original data. **This now needs to be tested in discrimination studies that exploit such continued data**. Note that the continuations entail no idealization or non-physical simplifications of responses predicted for higher observation points.

3. In conjunction with item 2, **sensitivities, minimum data and resolution requirements need to be determined for UC**. Here only very modest resolutions were employed, with no apparent ill-effect. Only ~ 10 cm point spacing was used in the processed data arrays, with underlying cross-track resolution really more like ~ 20 cm. Because UC signals were generated computationally using integral incorporation of equivalent sources, only the same undemanding resolution was required of the source distributions. This is much simpler and requires much less resolution that differential-equation-based calculation of upper or lower fields from measured boundary conditions. That said, surely some resolution constraints will apply. In the examples considered with a sharp clutter spike directly on a broader target signal pattern, the success of the method obviously depended on the system's ability to discern that the clutter produced a sharp divergence in signal value, i.e. a rapid change in value over space. Beyond this, fundamental uniqueness and

invertability questions regarding equivalent source distributions should be clarified beyond what was undertaken in this brief study.

4. The prospect that only quite modest arrays of equivalent sources may be sufficient for UC and strong clutter suppression indicates that **the method should be tested on data from such new instruments as those in SERDP project MM-1634 and ESTCP MM-0601**. The latter, for example, involves an instrument with a five by five array of rather large Rx loops, with inherently limited resolution. However, that may not be important for UC. The sensor also provides something of a blend of a mono-static data and the fully multi-static measurement as considered in this study. While the primary field is transmitted in sequence from different positions and is therefore changing, for each primary field a number of spatially distributed observations are taken. In the very least, we should investigate ways to transform data from both projects by superposition into an equivalent distributed response to a broad single excitation, ripe for UC.

5. This last point leads to the most inspiring, but also most challenging prospect, namely, **generalization of UC type clutter suppression to mono-static data, such as that from the EM-61, EM-63, GEM instruments**, et al. The formulations would have much in common with those generated here, but would also be fundamentally different in their meaning. If one obtains a distribution of mono-static signals over a plane, say, and then solves for an underlying distribution of equivalent sources over an arbitrarily deeper plane that will reproduce these data, he is really inferring an equivalent object below, not a boundary condition. That is, the inferred distribution of sources doesn't simply succeed in reproducing the values over a surface for a single field, and hence allowing calculation of the rest of the field (elsewhere). Rather, the equivalent source distribution over (say) the surface of the ground must somehow contain all the responsiveness of whatever physical sources are distributed in 3-D below the ground. For example, one might construct an array or continuous distribution over the ground of magnetic dipoles. Their responses would depend on the primary field locally striking them, which might be made to reproduce the responses of unknown objects below. At the outset, it is not at all clear that this can be done. Preliminary work done by our team using Normalized Surface Magnetic Charge (NSMC) [11-13] and related formulations has been suggestive however. Because the effective suppression of clutter offers such an enormous benefit,

this possibility should be investigated. Then many well developed discrimination methods for mono-static data can be applied much more effectively.

6. Not so well developed discrimination methods should be investigated as well. In particular, note that one virtue of the UC computations is that no model of a subsurface target is required. No laborious optimizations are required for target location, orientation, or properties in order to project the response to another elevation. One simply solves by direct computation for equivalent source distributions over an arbitrarily chosen surface below the data. This inspires the notion of further **"model-free" processing**, **leading beyond signal clean-up to UXO discrimination**. We have investigated such methods based on straightforward, robust integral measures of signal properties, such as total intensity combined with measures of spatial distribution. Analytical expressions, empirical relations, and fancier statistical learning machine experiments suggest that one can infer from these signal measures the basic target properties one needs for dig/ no-dig decisions: location and size of target. This kind of discrimination processing, which **requires no target model, optimization, or signal matching**, would be performed on the UC signal, which would be largely devoid of distortion due to clutter and noise.

2. Governing Physics and Mathematical Relations

Magnetometry and electromagnetic induction (EMI) sensors operate in the magneto-quasistatic regime (0 ~ 100's of kHz). Displacement currents are negligible [5]. Further, in our typically shallow UXO discrimination surveying, electric currents in the soil are some nine or more orders of magnitude weaker than those in targets of interest, so that the latter dominates the fields received by a sensor. This is because, according to the basic continuity laws of electromagnetics [5,6], electric fields in a metallic target and in the nearby soil are similar in magnitude. However electrical conductivity for UXO metals is on the order of 10^7 S/m, while that of the soil is likely to be at most $\sim 10^{-2}$ S/m [6]. Hence both electric and displacement currents are insignificant in the soil. Both currents types will also be negligible in the air, which possesses electrical conductivity that is much less than that of the weakly conducting soil [6]. Altogether, this means that, in the region where a sensor resides outside a metallic target, Ampere's Law in Maxwell's governing equations for electromagnetics [5,6] becomes.

$$\nabla \times \mathbf{H} \;=\; \nabla \times \left(\frac{\mathbf{B}}{\mu} \right) \;=\; 0 \tag{3}$$

For our purposes here, the magnetic permeability μ is constant and can be factored out of the equation. Thus both the magnetic flux intensity (**B** field, in teslas) as well as the magnetic field intensity (**H,** in A/m) are irrotational. That in turn implies that each can be expressed by the gradient of a scalar potential, i.e.

$$\mathbf{B} \;=\; -\nabla \Psi \tag{4}$$

Together with Gauss's law for magnetic fields

$$\nabla \cdot \mathbf{B} \;=\; q_\mathrm{B} \tag{5}$$

this implies a governing scalar Laplace equation.

$$\nabla^2 \Psi = -q_B \tag{6}$$

where physically the net magnetic charge density q_B is actually always zero. While nature does not permit the existence of isolated magnetic monopoles, i.e. positive or negative points of q_B, in some instances, as below, inclusion of this quantity via "equivalent" sources may prove to be a useful mathematical device. For example, the basic physically realizable magnetic source form is a dipole. While such a structure arises from electric current loops, it can be represented conveniently in regions away from the source by the pairing of positive and negative fictitious magnetic charges. These produce the correct fields in the sense that, in a region of interest away from the source, the fields satisfy the governing homogeneous version of (6) and the relevant boundary conditions. If q_m is retained as a source term, then the solution of (6) is [5,6]

$$\Psi(\mathbf{r}) = \int_{S_0} dS' \frac{q_B(\mathbf{r}')}{4\pi |\mathbf{r}\text{-}\mathbf{r}'|} \tag{7}$$

where S_0 is surface on which the equivalent charges reside and $\mathbf{r}$ is an observation point.

Overall, our instruments measure magnetic field, not potential. Given at least some vector components of $\mathbf{B}$ measured over a surface, one could in principle use the data as a boundary condition on (3) and (5), with $q_m = 0$, and then solve for $\mathbf{B}$ in the region above. However this presupposes rather complete, high resolution boundary data in $\mathbf{B}$, particularly if differential forms are applied. Finite differencing of the boundary data will generally be severely noise-amplifying. Various integral equation solutions for $\mathbf{B}$ above a measurement plane are also possible. In general, these also require manipulation of vector components of $\mathbf{B}$ and possibly derivatives or spatial transforms of those components to obtain the complete information needed.

The simplest and probably most robust way to express $\mathbf{B}$ is via (4) and (7),

$$\mathbf{B}(\mathbf{r}) = \int_{S_0} dS' \frac{q_B(\mathbf{r}')\hat{\mathbf{R}}}{4\pi R^2} \tag{8}$$

10   - -

where $\mathbf{R} = \mathbf{r} \cdot \mathbf{r}'$, $\hat{\mathbf{R}} = \mathbf{R} / |\mathbf{R}|$ and the equivalent sources do not reside *within* the region of interest although they may be on its boundary. This is an integral equation formulation, but in q_B, not in the sense of integral equation formulations only involving fields. A set of equivalent sources in (8) will inherently satisfy the divergence-free, curl-free requirements of our governing equations within the region of interest. If they further satisfy a legitimate boundary condition of that region then they provide all that one needs for complete definition of the field at hand.

In this study, only time domain (TD) instruments were used, so that $\mathbf{B}$ above is actually $\mathbf{B}(\mathbf{r},t)$. However, this is not significant. One can express the $\mathbf{B}$ distribution at any given time just on the basis of boundary conditions or source values at that same point in time. That is, time does not appear explicitly in (3) - (6). It only enters implicitly through forcing functions, i.e. boundary conditions or equivalently through q_B. The time and space scales in the MQS regime are such that there is no significant delay between changes through time on a boundary or in a source and those that result from them, some distance away. Altogether, noting that the formulation applies whether q_B is a function of time or frequency, we assume here that a time dependence is implied and suppress its expression in the equations.

Consider a distribution of charge q_B over a 2-D the surface S_0 (Figure 2), which in principle need not be flat. As these are equivalent sources, one may consider that they produce fields as if they resided in infinite homogeneous space, i.e. (8) applies without consideration of material properties, discontinuities, etc. The q_B could form a continuous function, or be a set of delta functions, as shown and as implemented computationally in this study.
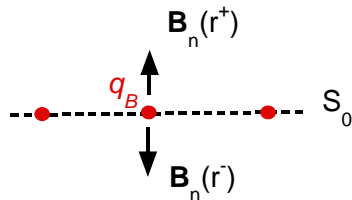
Figure 2. A source distribution of equivalent magnetic charges q_B over a flat surface.

Standard limiting arguments based on (5) [5,6] produce a relation stating that any jump in the normal component of **B** across the surface is equal to the magnitude of the source concentration on that surface. Thus, for a continuous distribution

$$B_n\left(\mathbf{r}^+\right) - B_n\left(\mathbf{r}^-\right) \;=\; q_B(\mathbf{r}), \quad \mathbf{r} \in S_0 \tag{9}$$

where $B_n\left(\mathbf{r}^+\right)$ and $B_n\left(\mathbf{r}^-\right)$ are normal field component values on opposite sides of the surface.

The source concentration at a point radiates equally in all directions, in particular equally into the regions above and below the surface. Thus, as suggested in the figure, $B_n(\mathbf{r}^+)$ and $B_n(\mathbf{r}^-)$ are equal in magnitude but opposite in direction, so that

$$q_B \;=\; 2\,B_n\left(\mathbf{r}^+\right) \tag{10}$$

If one can obtain sufficiently well sampled B_n values over a surface, this is very convenient for computing the field elsewhere as (10) is *pointwise* applicable. That is, given a B_n value at any point on the surface immediately allows the specification of q_B there without further solution. Information on this single field component over S_0 allows immediate inference of sources that are sufficient for all components of **B** beyond S_0. However, note that the component used must be the normal component, and the sources implied reside on the surface immediately adjacent to the positions where B_n was obtained. As explained in the next section, we obtain as data here the surface distribution of a **B** value component that is in a consistent but arbitrary direction relative to the surface normal. This does not allow us to infer directly, point by point as per (10), the value of q_B on the data surface.

To proceed nonetheless, consider an arrangement with magnetic field data **B(r)** on some measurement surface S_m, together with associated equivalent sources distributed on an offset surface S_0, as shown schematically in Figure 3.
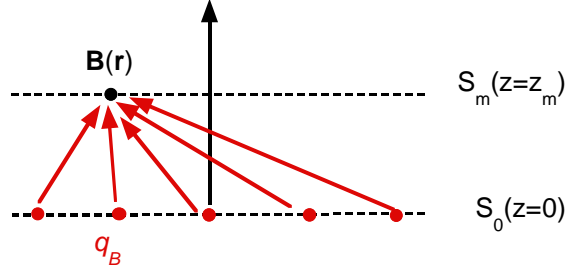
Figure 3. Charge sheet offset from observation (data) point.

In contrast to the relation in (10) in which the charge value at a single point implies the value of a **B** component there, here all charges contribute to each point value of **B**. If the charge distribution is correct (i.e. such as would be obtained from (10) *applied on* S_0), it will provide all components of **B** on S_m. Conversely, if any of the **B** components is changed over S_m, that must imply some change in the q_B. Thus, from data on an offset surface one should be able to solve for the underlying q_B on S_0 using any consistent distribution of values for a given component of B. Readers left a bit queasy by this rather sketchy treatment of uniqueness issues are referred to comments elsewhere in this report. As presented thus far, these remarks may at least serve as an informative context and motivation to follow the computational procedures successfully applied in the project.

When a component of the response **B** field in some arbitrary $\hat{\mathbf{B}}_e$ direction constitutes the data, (8) provides the signal as,

$$S\left(z = z_m\right) \;=\; \int\limits_{S_0(z=0)} \mathrm{d}\,S' \; \frac{q_B\left(\mathbf{r}'\right)\hat{\mathbf{B}}_e \cdot \hat{\mathbf{R}}}{4\pi R^2} \tag{11}$$

which is discretized computationally as

$$S_i \;=\; \sum_{j=1}^{J} \frac{q_{B_j}\,\hat{\mathbf{B}}_e \cdot \hat{\mathbf{R}}_{ji}}{4\pi R_{ji}^2} \tag{12}$$

13   - -

The source distribution in (11) has been treated as a collection of delta functions in space, of magnitude q_{B_j} at $\mathbf{r}'_j$; S_i is the signal at $\mathbf{r}_i$ and R_{ji} is the distance from $\mathbf{r}'_j$ to $\mathbf{r}_i$.

Lastly, let us note an important distinction regarding the kind of data that can be treated in continuation calculations. Most EMI instruments enlisted for UXO discrimination studies or field work produce at least approximately *mono-static* data. That is, the signal is received at the same location from which the primary (excitation) field is transmitted. This means that, as the sensor is moved around an object below ground, each observation represents a view from a different position of the target's response to excitation *from that position*. Thus each recorded response is a sample of a different response ("secondary") field. This is fundamentally different from the situation that we have considered thus far and will consider everywhere below. In particular, we assume that the excitation field is invariant in the sense that it does not change as a result of different observation positions of the instrument. In traditional, static magnetometry the excitation field is the earth's field. On the time and space scales of our surveys, this may be regarded as constant.

In our field studies in which continuation is applied (to our knowledge) for the first time to transient EMI data, the excitation field is provided by a large loop surrounding the entire site. Its excitation field is unchanged as surveyors change position to observe the response field. In either this case or that of static, traditional magnetometry, around a given target all data consist of different samples of *the same* response field, which may vary in magnitude and direction from point to point. Thus, a sufficient sampling of this field over space can provide a legitimate boundary condition on it, or would allow computation a set of equivalent sources that would serve the same function. By contrast, a distribution of mono-static EMI data over a surface (e.g. from an EM-61 or GEM-3 instrument), no matter how complete or well resolved, does not comprise a sufficient boundary condition in the usual sense. One could not use such mono-static data to compute data values elsewhere, at least as described above. Details of the fully multi-static observations engaged here are presented in the Section 3.2.

2.1.   Nature of the TD Magnetometer Data

The time domain (TD) GAP Geophysics system [8], developed from the Sub-audio Magnetics technology, functions by surrounding a field of as much as several acres with a transmitting (Tx) loop. Responses from objects within that area constitute the secondary field, measured via local roving magnetometers. While the receivers register a time dependent signal, they are nonetheless magnetometers of the sort used in static magnetometry. However here, instead of an essentially invariant earth's field serving as the excitation, the imposed on-off Tx loop current provides a single, large primary field that does not vary appreciably over the space around the targets. Decaying target responses are recorded during the off phase of the Tx currents, when the excitation field is negligible. Despite its TD character, the transient GAP data has fundamental links to the earth's field in a manner reminiscent of traditional magnetometry data. This results from a combination of the receiver type and the fact that, while the Tx current is off during the recording time, the earth's field is not.

The cesium type magnetometer receivers in the GAP system respond fundamentally to the *magnitude* of the *total* magnetic field that impinges upon them. That is, the resonances in the receiver respond to the total $|\mathbf{B}(t)| = \sqrt{B_x^2(t) + B_y^2(t) + B_z^2(t)}$ including the earth's field. However, continuation calculations require at least partial information on individual vector components. If one begins with an equation such as (8) but manipulates it so as to proceed in terms of $|\mathbf{B}|$ instead of $\mathbf{B}$ or its components, the problem becomes nonlinear. In addition to adding much complexity, the optimizations required to solve for the q_B would be vulnerable to non-uniqueness problems as well. In practice, as explained below, the inclusion of the earth's very large field in the raw data compensates for added complexity by allowing some beneficent approximations [9], which in turn permit one to proceed with continuation.

The perturbation field, **b**, produced by the target of interest in response to the GAP Tx field is much smaller than the earth's field, $\mathbf{B}_e$.

$$Earth's\ field\ magnitude\ =\ |\mathbf{B}_e|\ =\ B_e\ \gg\ b\ =\ |\mathbf{b}|\ =\ anomaly\ magnitude \qquad (13)$$

The signal *S* from the GAP receivers consists essentially of the magnitude of the earth's field plus the perturbation, minus the magnitude of the earth's field alone.

$$S = |\mathbf{B}_e + \mathbf{b}| - B_e \tag{14}$$

Figure 4 shows the vectors involved. This is only a schematic diagram in that the origin is substantially farther away than is depicted, so that the two vectors containing the earth's field are longer and more parallel to each other than is shown. In any case, even as the figure appears, one sees geometrically that the signal consists effectively of the projection of the perturbation **b** onto the direction of the earth's field.
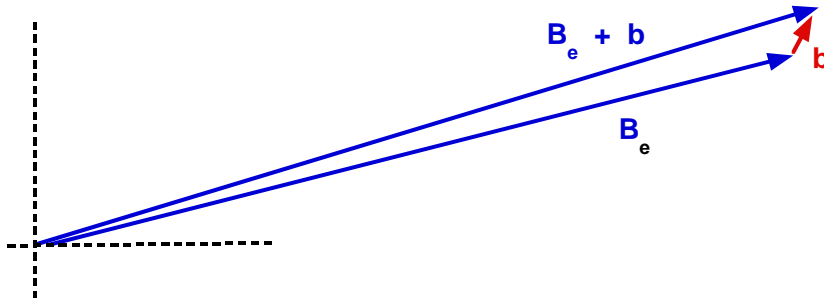
Figure 4. Schematic vector diagram of the field impinging on the receivers, consisting of the earth's field with and without the target perturbation **b**.

Expressed in equations,

$$|\mathbf{B}_e + \mathbf{b}| - B_e = \sqrt{(\mathbf{B}_e + \mathbf{b}) \cdot (\mathbf{B}_e + \mathbf{b})} - B_e$$

$$= B_e \sqrt{1 + 2\hat{\mathbf{B}}_e \cdot \mathbf{b}/B_e + b^2/B_e^2} - B_e \tag{15}$$

$$\approx B_e \sqrt{1 + 2\hat{\mathbf{B}}_e \cdot \mathbf{b}/B_e} - B_e$$

$$\approx B_e \left(1 + \hat{\mathbf{B}}_e \cdot \mathbf{b}/B_e + h.o.t\right) - B_e \approx \hat{\mathbf{B}}_e \cdot \mathbf{b}$$

where the higher order terms (*h.o.t.*) in the Taylor series are easily neglected. With the data consisting essentially of the component of the perturbation field in the earth's field direction, $S =$

- -

b_e, the governing equation just becomes (11), i.e. numerically (12). This is the relation used in all the computations that follow. A value for $\hat{\mathbf{B}}_e$ applicable at Aberdeen Proving Ground testsite was obtained from the USGS [http://geomag.usgs.gov/], which furnishes detailed data, charts, and models easily capable of producing more accurate values than are needed here. Using the IGRF-2005 model from that source for 6/15/2007, lat 39N31 = 39.5167, long = 76W08 = -76.13 produces components of the earth field

$$
\begin{aligned}
B_{e,x} &= 20{,}149 \text{ nT} \\
B_{e,y} &= \text{-}4{,}092 \text{ nT} \\
B_{e,z} &= 48{,}437 \text{ nT}
\end{aligned}
\tag{16}
$$

which, when translated into the coordinate system used in the analyses (X positive north, Z positive up), produces

$$
\hat{\mathbf{B}}_e = [\text{-0.0778, 0.3830, -0.9205}]
\tag{17}
$$

3. Upward Continuation

3.1. Simulations

Prior to field testing, simulations were performed to assist in algorithm development; to validate the concepts and computer codes; and to identify problems and assess the usefulness of the approach, especially for clutter suppression. A target and a nearby clutter item were assumed to behave as anisotropic point magnetic dipoles, producing responses according to the relation

$$
\mathbf{H}^s\left(\mathbf{r}_m\right) = \frac{3\hat{\mathbf{R}}_{tm}\hat{\mathbf{R}}_{tm} - \mathbf{I}}{4\pi R_{tm}^3}\cdot\mathbf{m}_t + \frac{3\hat{\mathbf{R}}_{cm}\hat{\mathbf{R}}_{cm} - \mathbf{I}}{4\pi R_{cm}^3}\cdot\mathbf{m}_c
\tag{18}
$$

- -

where $\mathbf{H}^s$ is the secondary field at a measurement point $\mathbf{r}_m$; the subscript "tm" indicates target-to-measurement point, while "cm" indicates clutter item-to-measurement point; and $\mathbf{m}_t$ and $\mathbf{m}_c$ are the induced target and clutter dipole moments, respectively. The primary field that stimulates $\mathbf{m}_t$ and $\mathbf{m}_c$ does not appear explicitly in the expressions because, as in the field setting, it is essentially uniform and vertical. We assume that the clutter item has an inherently smaller dipole moment than the larger target but that its signal obtrudes because it is shallower. The signal pattern is complicated as well by the fact that it is sampled in a generally oblique $\hat{\mathbf{B}}_e$ direction, as per (11). This can cause changes in signal sign from one side of the target to the other even although the secondary field is largely vertical. Figure 5 show signal contours for a hypothetical situation in which $\mathbf{m}_c = [0,0,10^{-1}]$, $\mathbf{m}_t = [0,0,1]$, and the measurement plane is at Zm = 0.2 m. The target is beneath the origin at z = -0.6 m while the clutter item is shallower and is offset, i.e. $\mathbf{r}_c = [0.5, 0.5, -0.2]$ m. The contrast between the top and bottom plots shows the asymmetries introduced by the $\hat{\mathbf{B}}_e$ sampling of $\mathbf{H}^s$ relative to what one would see just by apprehending the vertical field component.

Figure 6 shows an upward continuation test for this situation. The top plot shows again the data on the measurement plane, i.e. $\hat{\mathbf{B}}_e$ component of the secondary field at Zm = 0.2 m. The signal that would be obtained at Z = 0.4 m is also computed directly from the two actual sources (middle plot). The bottom plot is obtained by first solving for a plane of equivalent sources q_B at Zq = 0 using (12), based on the data S at Zm shown in the top plot. This q_B solution is then used to compute the field at Z = 0.4 m. Clearly the upward continuation solution does well in predicting the signal at a higher elevation. Equally important, both actual and continuation plots show a notable diminution of the prominence of the signal from the shallow clutter item.
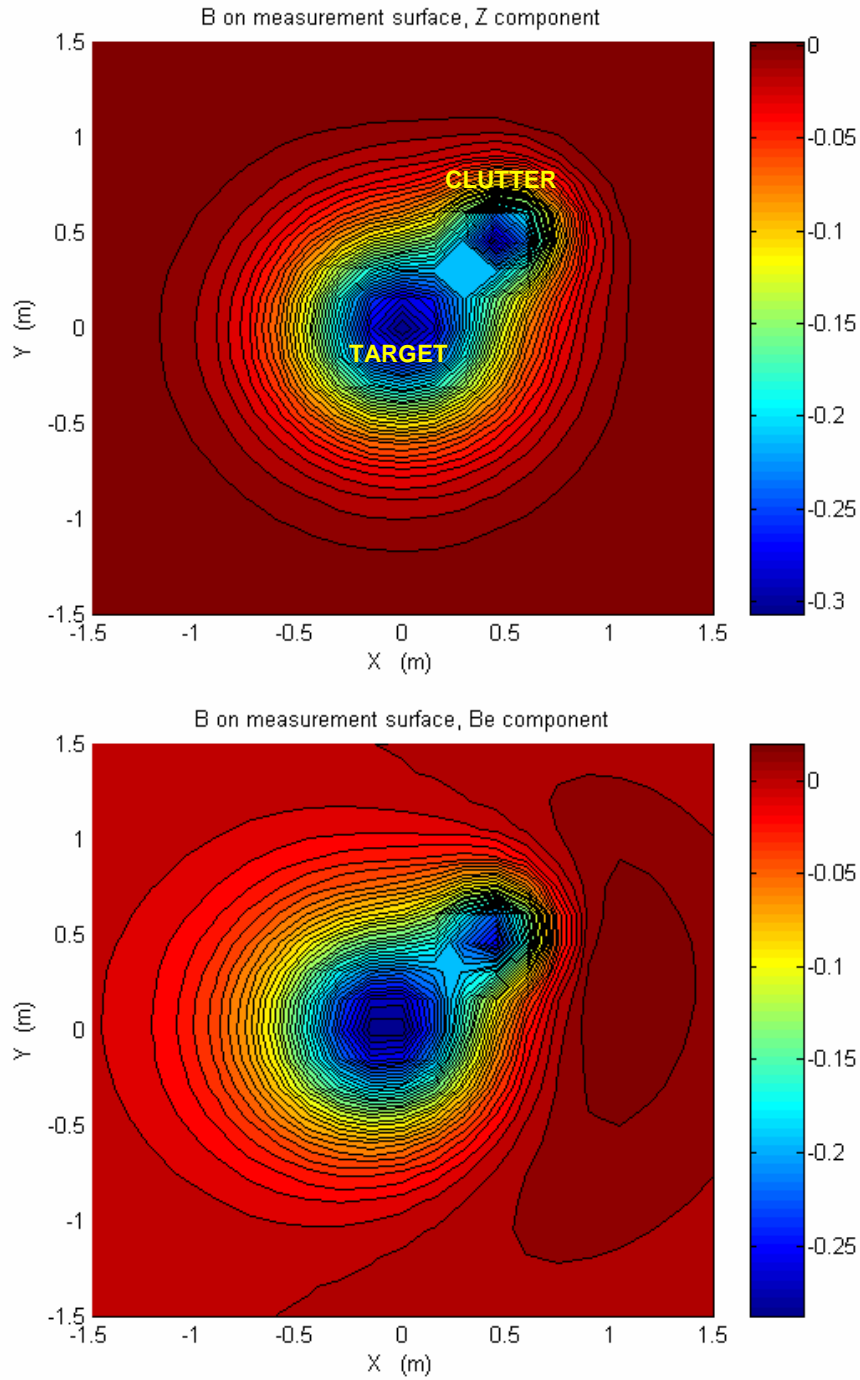
Figure 5. Simulated responses of a target and clutter item combination, when $\hat{\mathbf{B}}_e$ is just $\hat{\mathbf{z}}$ (top), and when $\hat{\mathbf{B}}_e$ is [-0.0778, 0.3830, -0.9205] as per the APG site (bottom).
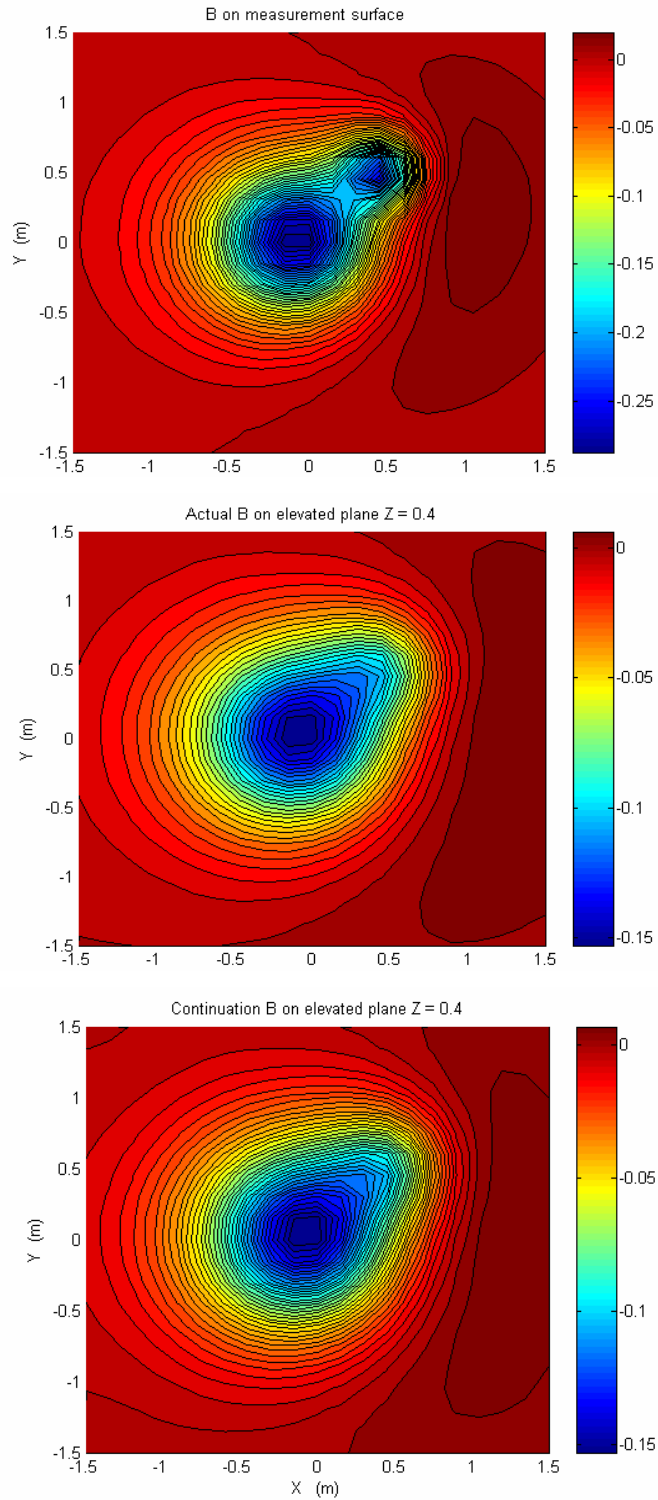
Figure 6. Same case as in Figure 5, showing $\hat{\mathbf{B}}_e$ component of $\mathbf{H}^s$. Top: Data on measurement plane (Zm = 0.2 m). Middle: actual signal that would be obtained at a higher elevation (Z = 0.4 m). Bottom: Continuation signal computed for Z = 0.4 m.

In these computations the dimensions of S_0 were the same as those of S_m (see plots). Spatial increments between points in the square arrays of data and of sources were the same, 0.15 m, being only slightly less than the separation between S_0 and S_m. While this discretization is rather coarse, it still works well and is chosen purposely to avoid ill-conditioning. With a condition number of ~ 75 one would expect distortions in q_B when noise at the level shown in Figure 7, top, is added (See Section 5). Here *RelNoiseMag* = 0.25, where that parameter implies added white noise between +/-*RelNoiseMag*/2 times the signal maximum. While distortions in q_B may indeed occur, the bottom plot shows that to a remarkable extent their effects are integrated out in the course of the upward continuation: resemblance between magnitude and shape of the signal distributions in the middle and bottom plots is clear. Thus the q_B solution and continuation process together appear quite robust in the fact of substantial noise in the data. *Both random noise as well as physical clutter signals are suppressed by the process.* Figure 8 pursues this, with somewhat more moderate noise (*RelNoiseMag* = 0.1) and $\mathbf{m}_t = [0,1,1]$ for a more complicated response pattern. The system still works equally well.

Of course, in all this we are primarily interested in isolating the signal from the target itself. Figure 9 illustrates the difference between a signal on the data plane from the target alone, compared to that from the combination of target, shallow clutter item, and random noise. When upwards continuation processing is applied to the noisy and cluttered data, the results in Figure 10 are obtained. Continuation has done a good job of predicting the signal from target and clutter item at considerable elevation. While the magnitude from this combination is still slightly high relative to that from the target alone, the differences are minimal. For all practical purposes, the method shows promise for isolating target contributions in a cluttered, noisy signal.

As mentioned above, noise in the data can distort the q_B solution, but in the examples here that did not ultimately impact the quality of upward continuation significantly. The distortions are still worrisome, however, in that under some other circumstances they could carry through to the continued signal. Further, if one wishes to examine the q_B solution itself, the distortions could be problematical. The distortions in q_B can be especially prominent when one chooses geometrical parameters different from those above, most notably deeper S_0, as for the downward computations that are one investigatory focus of this project. Figure 11 shows the q_B solution obtained in the problem we have been examining, with and without noise added to the data (*RelNoiseMag* = 0.1). In that the continuation results are good, the essential source distribution is clearly buried within the heart of the distorted solution, whose rapid oscillations are ultimately

integrated out in the continuation integration (12). Nevertheless, the lower q_B plot is not a pretty picture. Especially if distorted further, its pattern would be difficult to interpret and its errors could threaten the quality of upward inferences. Section 5 discusses the nature, origins and control of such distortions.
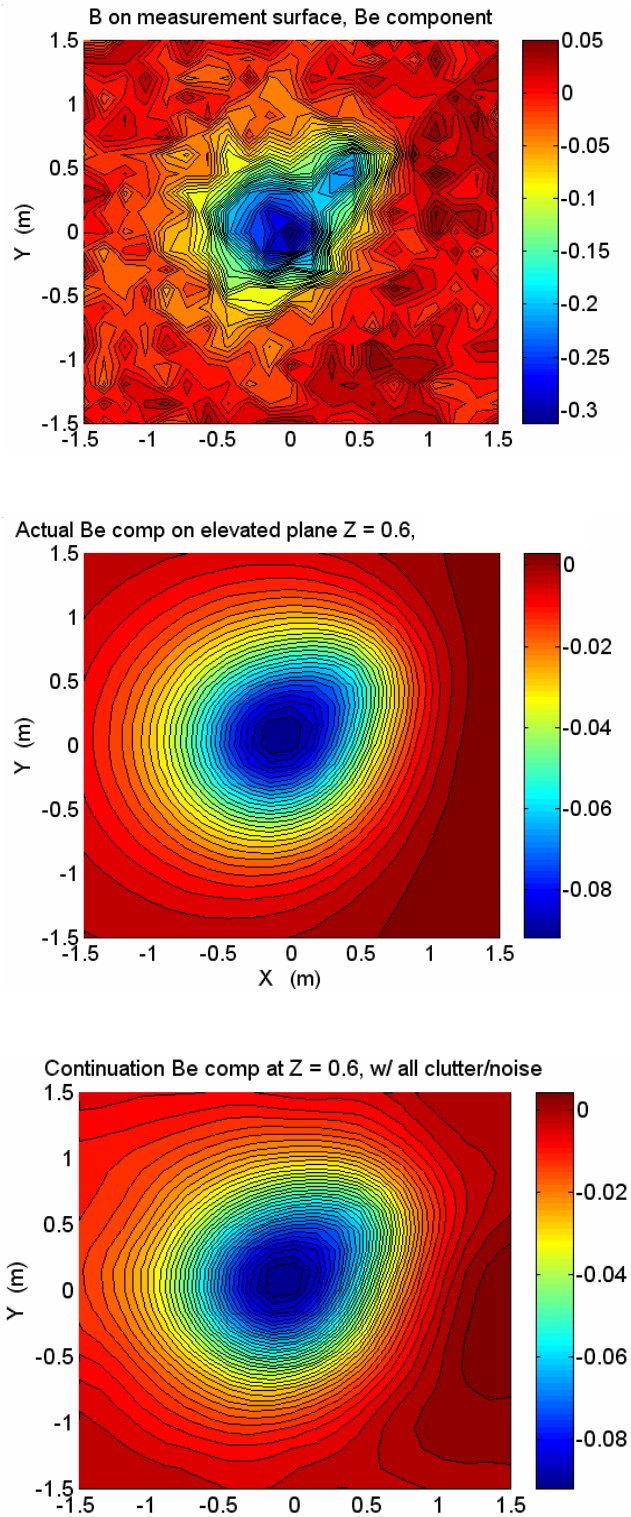
Figure 7. Same case as above but with *RelNoiseMag* = 0.25. Top: Data on S_m at $Zm = 0.2$ m. Middle: Actual signal from targets, without noise, at $Z = 0.6$ m. Bottom: Signal at $Z = 0.6$ m obtained by continuation from q_B based on data in top plot.
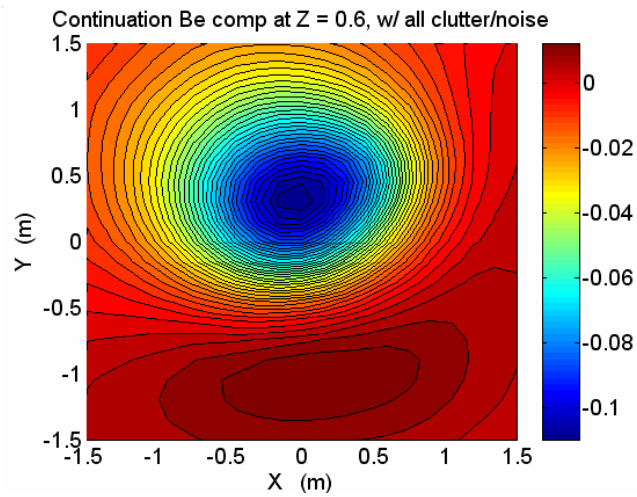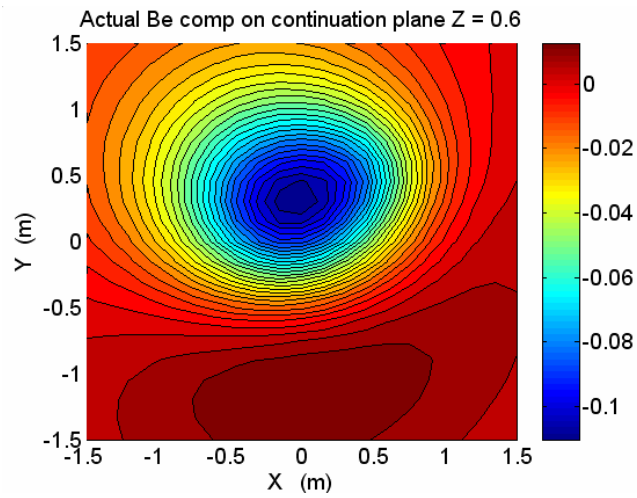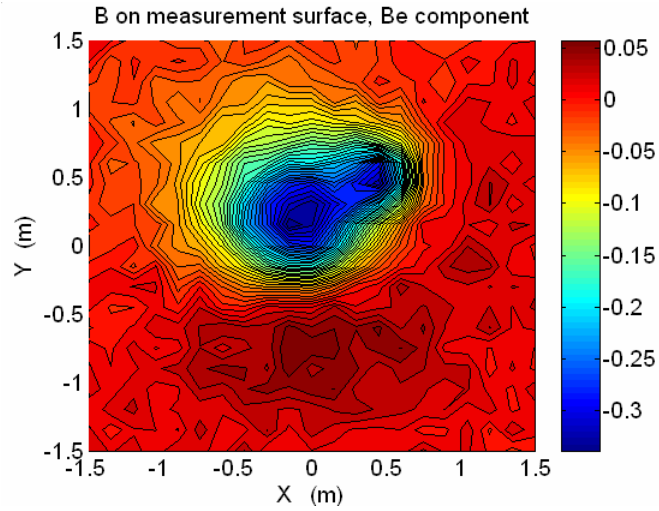
Figure 8. Same as previous plot, but with *RelNoise* = 0.1 and $\mathbf{m}_t = [0,1,1]$.
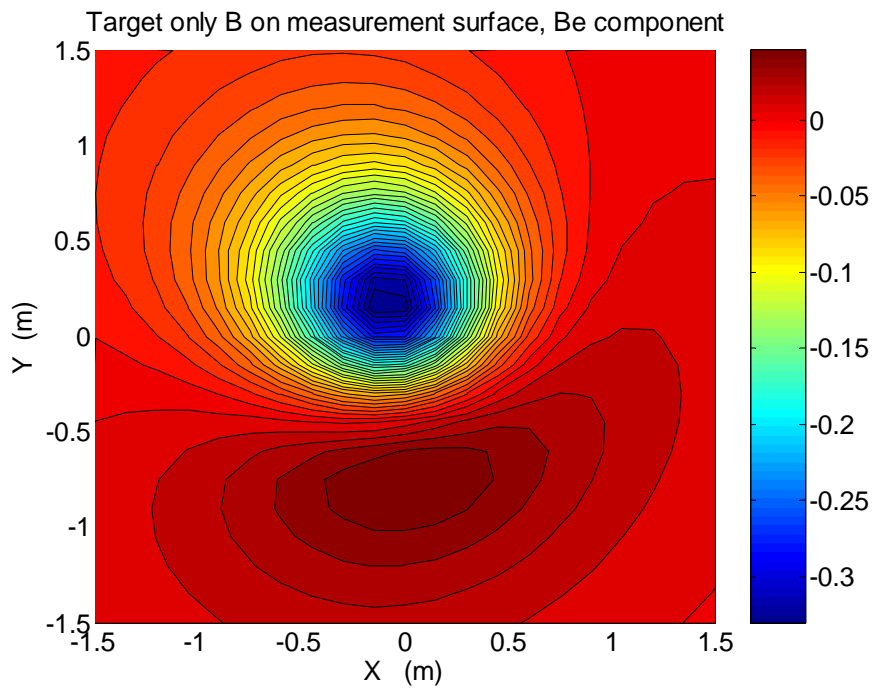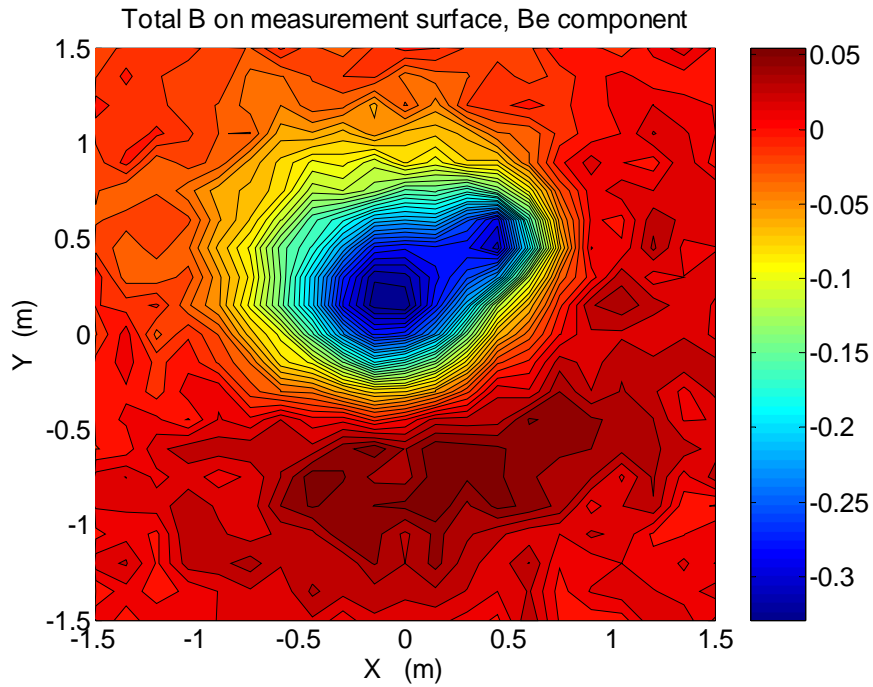
Figure 9. Same in previous figure but showing difference between data with noise and also clutter item (top) and from target only (bottom).

Actual Be comp on continuation plane Z = 1.2, no clutter/noise

Actual Be comp on continuation plane Z = 1.2, w/ clutter, no noise

Continuation Be comp at Z = 1.2
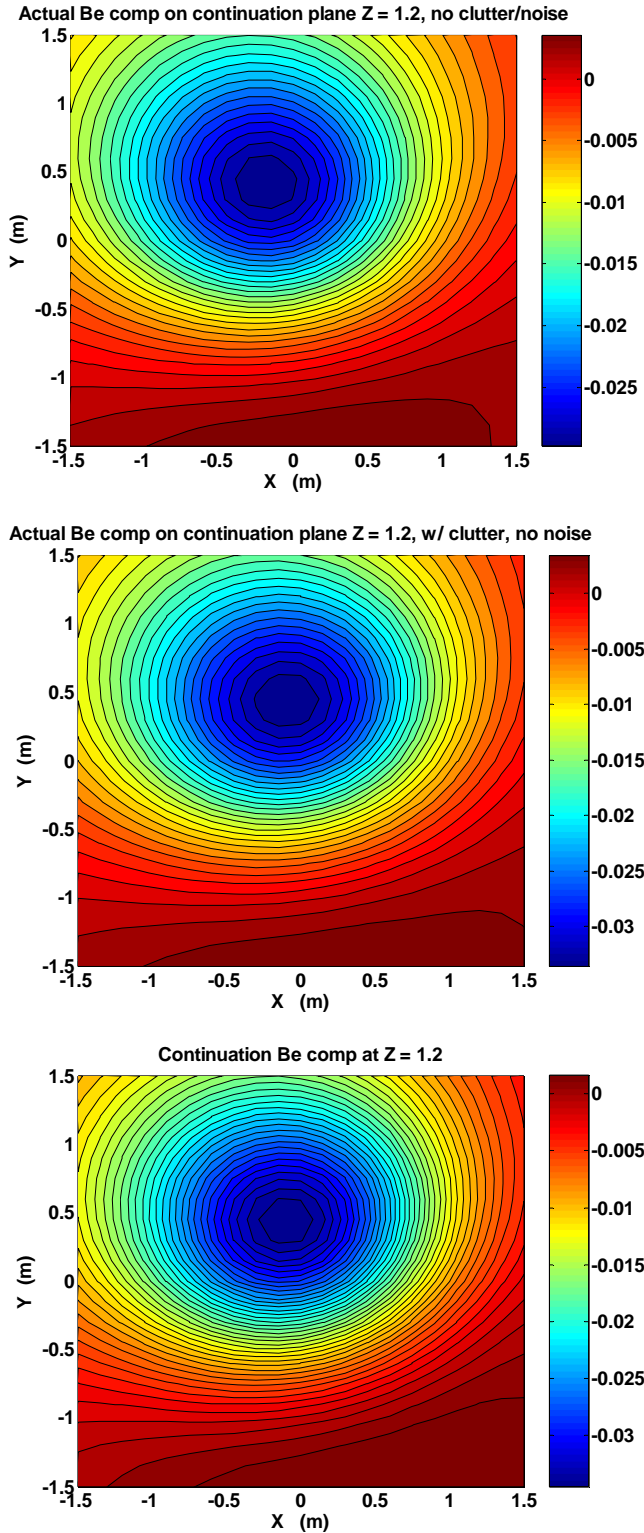
Figure 10. Same parameters as in Figure 9, showing little difference at elevation between theoretical target-only signal (top), that from the target plus clutter (middle), and that from continuation using target + clutter + noise on the data plane (bottom).
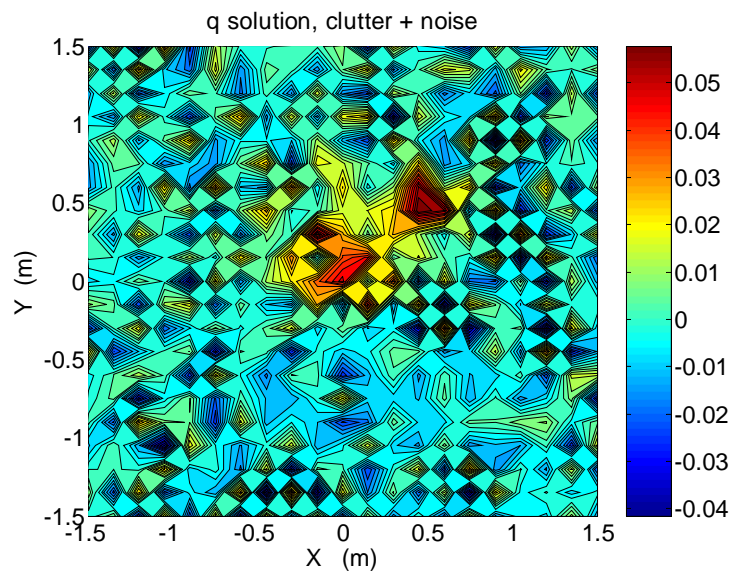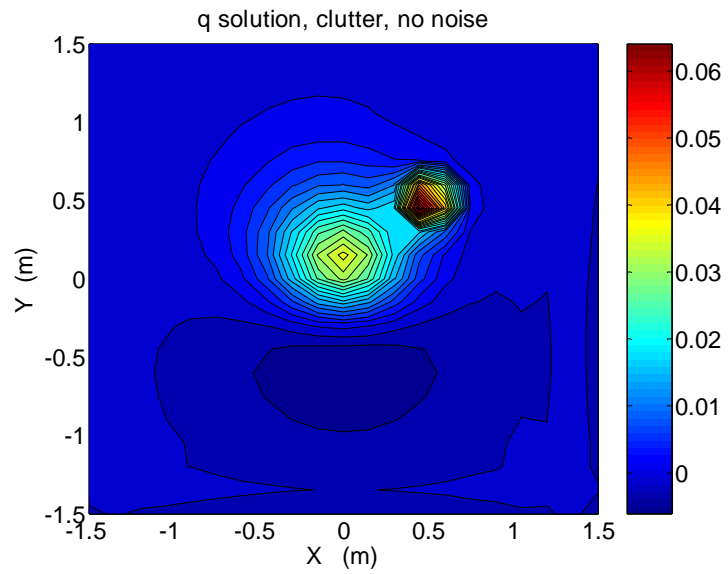
Figure 11. The q_B solution for the same case but with *RelNoiseMag* = 0 (top) and *RelNoiseMag* = 0.1 (bottom).

3.2.   Field Tests

During June 2007 the team made measurements with the GAP Geophysics survey system [8] at the UXO Standardized Test Site at Aberdeen Proving Ground (APG). A section of field approximately 40 m square was surrounded by the transmitter coil and measurements were made within it along lines over an area approximately 4 m by 9 m. The wheeled rig proceeded along lines guided visually by taught strings. Figure 12 shows the rig proceeding along a line and the pattern of receiver positions along all the lines. The rig transported four receivers spaced 38 cm apart. Lines were spaced so that the sensor tracks were interleaved, producing on average an approximately 19 cm data spacing in the across track direction. Data along track were taken approximately every 0.3 sec which, with the slow rate of progress maintained, meant a 1 to 2 cm data density in the along track direction.
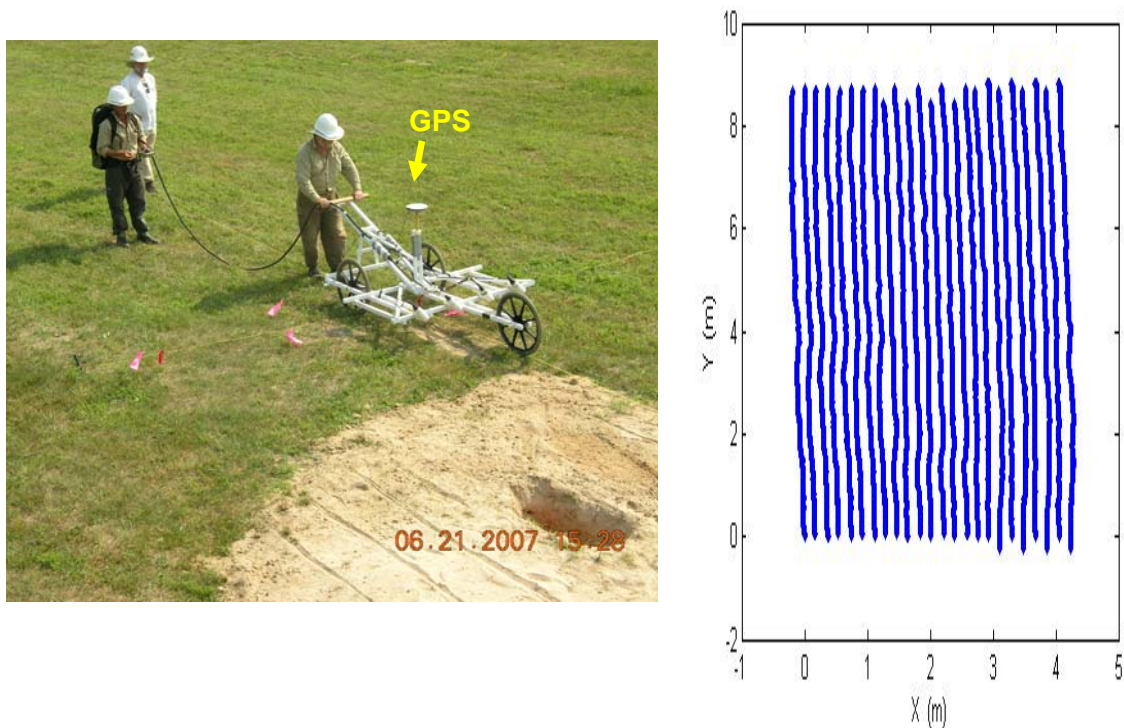
Figure 12. Left: survey rig proceeding along a survey line across the edge of the sand pit in which targets were buried. Right: the paths of the individual receivers.

Targets were buried in about the center of the sand pit (hole in Figure 12, close up in Figure 13). Primarily, a 105 mm projectile was used in various horizontal, vertical, and inclined orientations.

Figure 13. Hole dug in sand pit with 105 mm projectile placed horizontally at bottom and clutter item (shotput) on surface, with meter measure.

Positioning data was provided by a GPS antenna attached to the rig, indicated in Figure 12 and Figure 14. This was elevated above the receiver platform to avoid electronic interference. It was lowered from its initially high position (Figure 12) to that in Figure 14 in order to minimize positional error due to tilt of the platform on the uneven ground. Examination of the data along the lines suggests a residual random error from platform motion of about 1 or 2 cm.

As the data density along and across track are quite different, a specialized interpolation algorithm was devised to produce 2-D grids of data with uniform spacing in both horizontal directions. While data produced by the algorithm should not possess any greater positional error than the original, it will not be improved either. This should be born in mind when interpreting plots such as the example signal in Figure 15. Drawing contours (i.e. via Matlab) can produce an illusion of isotropic resolution, but examination of the horizontal vs vertical patterns in the plot reveals the remains of the originally unequal data densities.
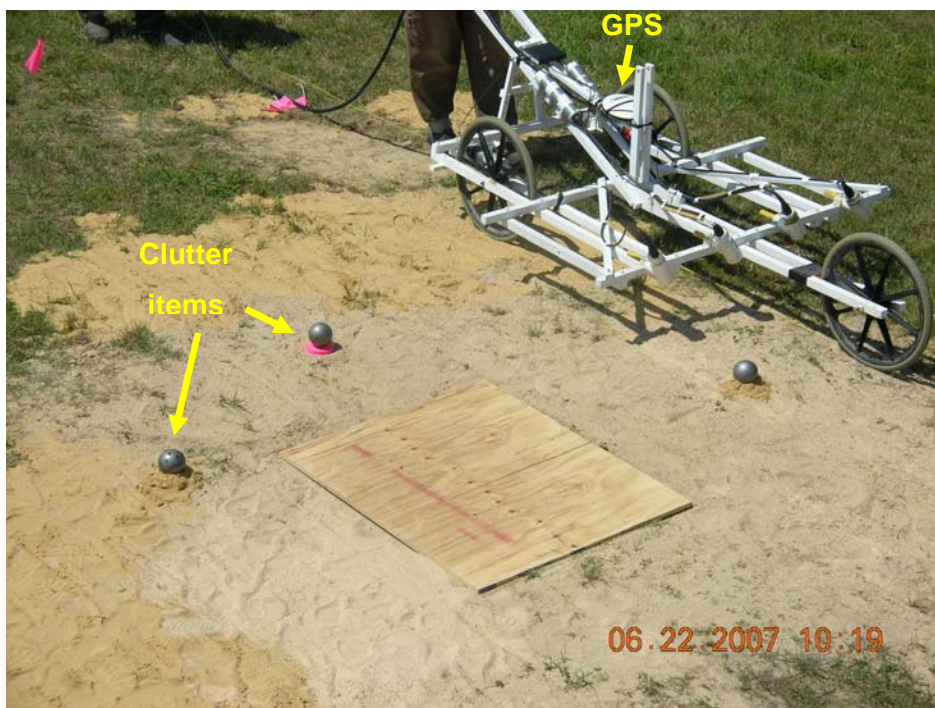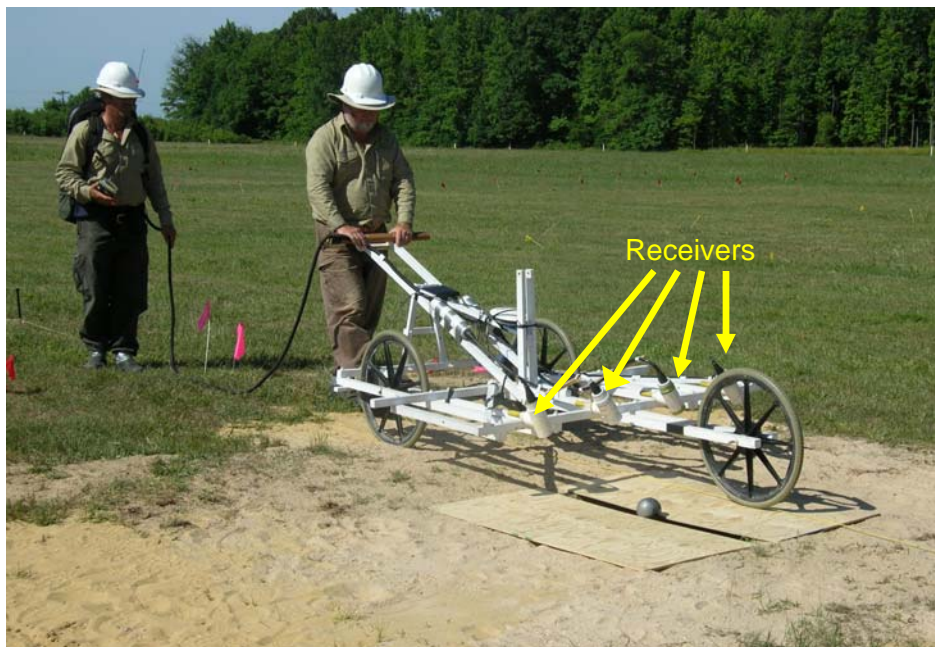
Figure 14. Rig passing over target region, with target hole covered by plywood and one (top) or three (bottom) shotputs placed nearby to serve as shallow clutter items.

Data at Z = 0.15
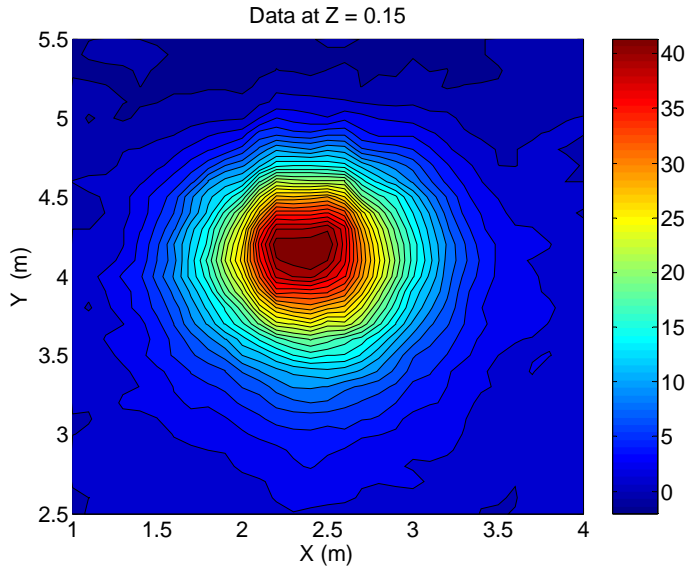
Figure 15. Data from lines such as those in Figure 12 interpolated onto a square grid of points at 10 cm x-y spacing.

The spatial distributions of data such as that in Figure 15 pertain to a particular point in time. At any given point in space, the sensor's receivers see a time pattern of magnetic fields illustrated in a plot of field data in Figure 16, top, from a relevant portion of the on-off Tx cycle. The earth's field contribution has been subtracted. When the voltage in the Tx cable is switched on, before time zero, the current and consequent Tx field rise to an essentially flat, high value, which gradually saturates the target. When the Tx voltage is shut off at time zero, the primary field decays rapidly until only the secondary field from the target remains at the receiver. The log-log decay of the latter is shown in Figure 16, bottom. Note that the magnitude of the earth's field is ~ 50,000 nT. The magnitudes of signals shown in Figure 16 validate the assumption that the signals of interest - the perturbation quantity **b** above - are indeed much, much smaller than the ambient earth's field. The first time gate in the plot and in data analyzed is chosen to be late enough to avoid distortions associated with the lingering decline of the primary field in earliest time after zero. In all analyses here, which pertain to spatial distributions of signals at a given time, it does not matter much in principle what time point is chosen during the decay in Figure 16, bottom. In an actual survey one might wish to examine later time points at which responses of smaller clutter items might well have diminished, relative to that from larger items of interest. To retain focus on clutter vs target signals, it behooves us here to use early time points where both

signals are at their clearest. Therefore in all treatments of field data below we choose a time gate at 0.625 ms after time zero.
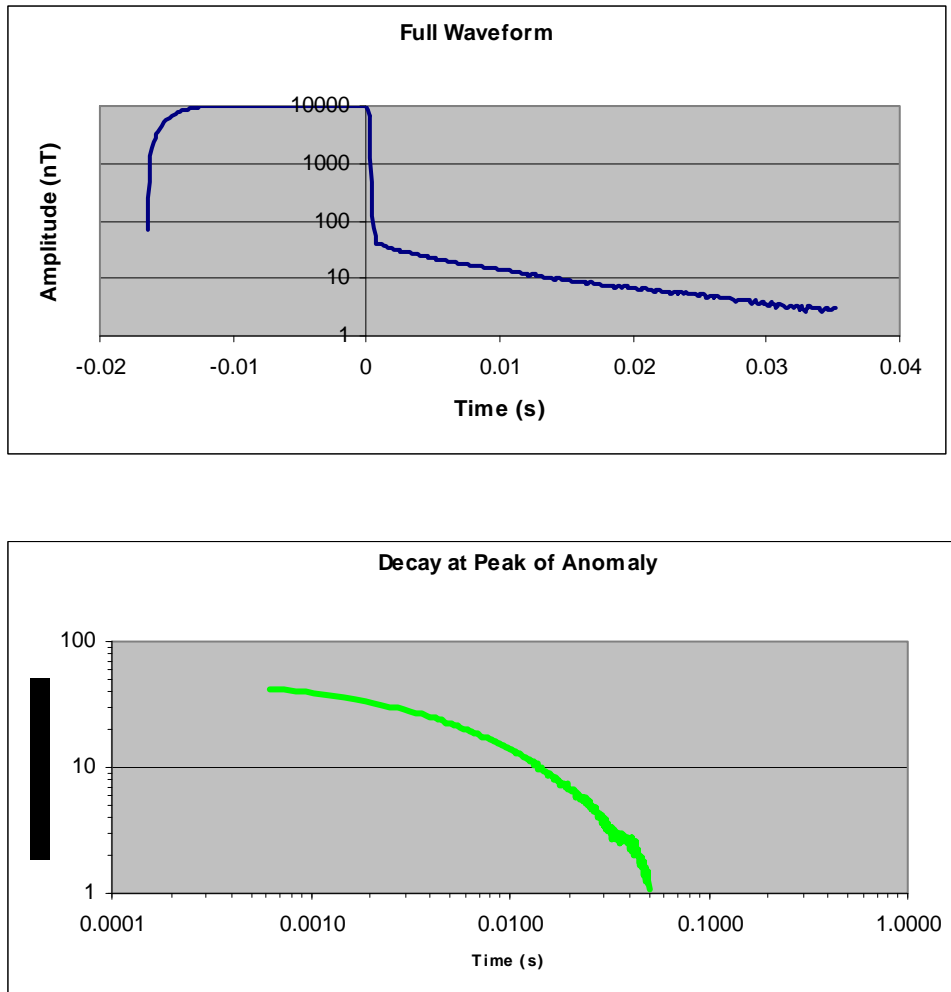
Figure 16. Data taken over the peak of the target signal for a 105 mm projectile buried 73 cm below the sensor. Top: In linear time, full waveform including Tx field prior to time zero, rapid decline after shutoff, followed by slow decay associated with target. Bottom: Decay of the target, isolated, relative to log(t).

The level of inherent noise in the data might be best apprehended from the plots of individual receiver outputs along the survey lines (Figure 17) rather than by examination of interpolated values in Figure 15. Not surprisingly, the relative magnitude of the noise is more or less inversely proportional to the overall signal strength. In general, relative to peak data values (Figure 17, top), the SNR is good.
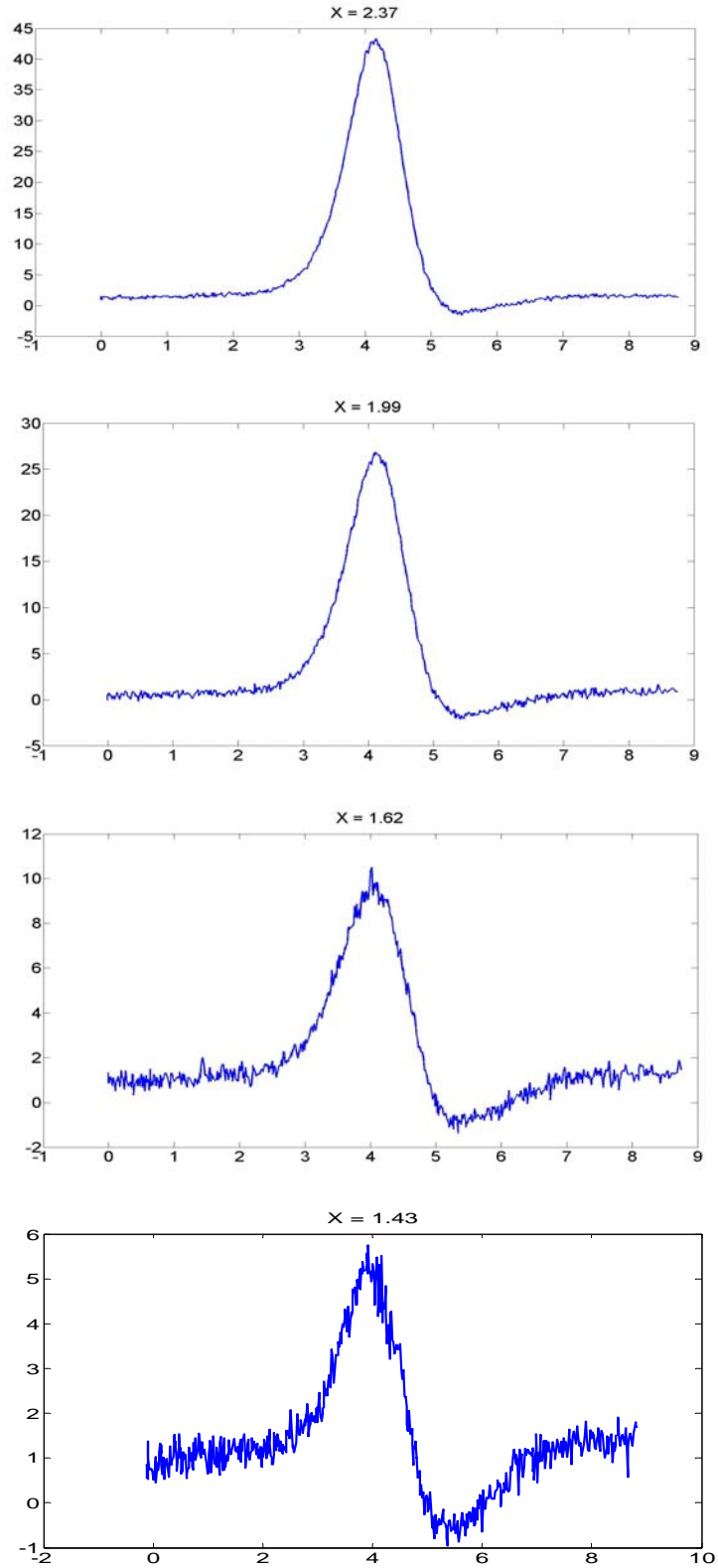
Figure 17. Data along survey lines over a vertical buried 105 mm UXO for the same case shown in Figure 15, illustrating the level of noise.

- -

For a first look at upward continuation of field data, consider the case of a vertical 105 mm projectile buried initially 73 cm to its shallowest point below the sensor (Figure 18). In all cases, because it was impractical to redo surveys with the sensor raised to a higher elevation, instead the same thing was accomplished by placing all targets deeper (soil response was not significant). At the initial distance between sensor and target, some of the apparent lateral (x-direction) spread of the signal in the top plot is caused by the rather large separation of the survey lines in that direction and interpolation of values in between. In any case, when the sensor-target distance is increased to 96 cm, the response is more clearly centered and also more broadly spread (middle plot). Continuation computations for the 96 cm separation, based on the initial 73 cm data, are shown in the bottom plot. Continuation catches all the essentials of the actual elevated measurements in both magnitude and spread of the signal, in the process filtering out a good deal of random irregularity in the signal.

The quality and resolution of the data in this example and our ability to institute only modest changes in sensor elevation above the target limit the appeal of this example as a demonstration of the technique and its benefits. Computations further below exploit the real appeal of the method, namely, its ability to project data to separations that could not be attained in the physical tests with consequent substantial benefits of clarity. Remaining for the moment with more modest changes in separation for the sake of validation, some results involving clutter are illuminating. Figure 19 shows a case in which a single shotput was placed at ground level to serve as a clutter item. At the initial elevation, both clutter and UXO are approximately equal in magnitude. When the sensor-target distance is increased (middle plot) signals from both sources decline, but the strength of the clutter signal fades relative to that from the UXO. This is reproduced in the signal obtained by upward continuation (bottom plot). The projected magnitudes are approximately correct, while the patterns are actually cleaned up. Continuation calculations will reproduce most of the signal irregularities in the original data (see next example). However, upward continuation will tend to iron these wrinkles out, for good physical/mathematical reasons. At the same time, actually obtaining signals with the sensor at greater distances overwhelms this physical effect, as target signals become weaker relative to any irreducible background noise/ clutter.
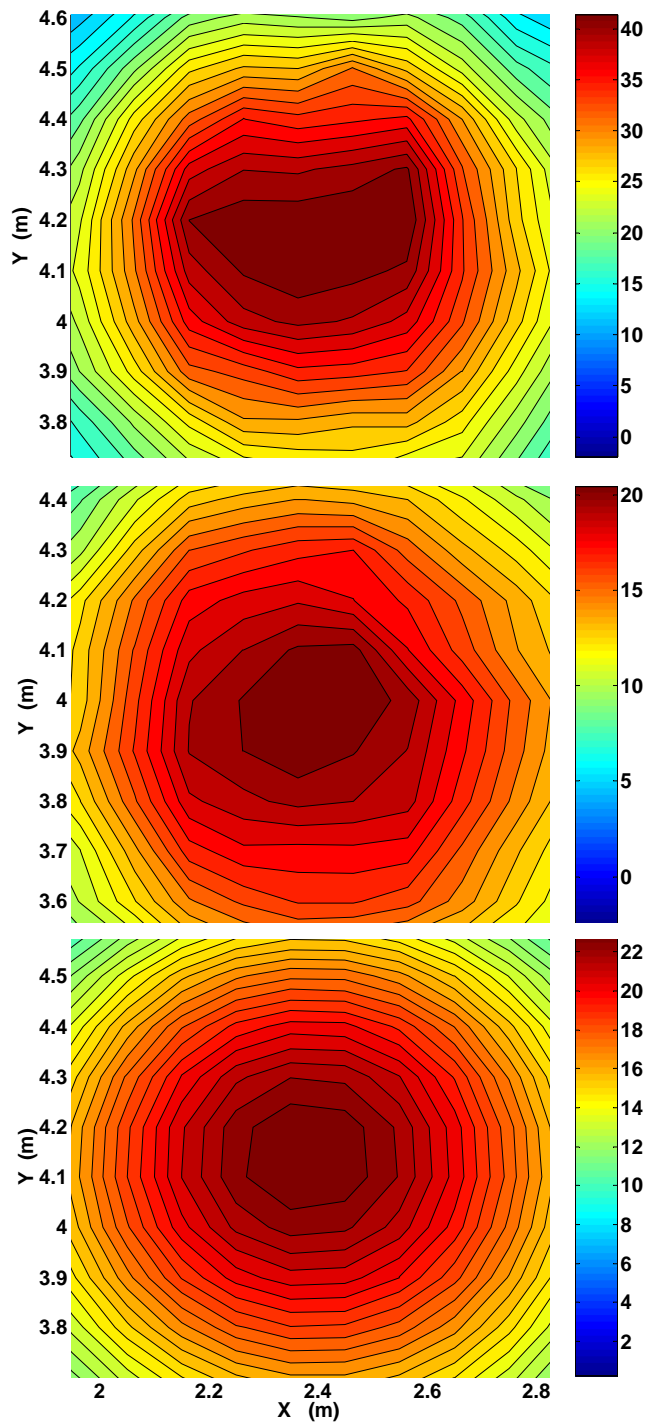
Figure 18. Signal from a vertical 105 mm UXO. Top: Data at d = 73 cm. Middle: Data at d = 96 cm. Bottom: projection from data at 73 cm to signal at 96 cm.
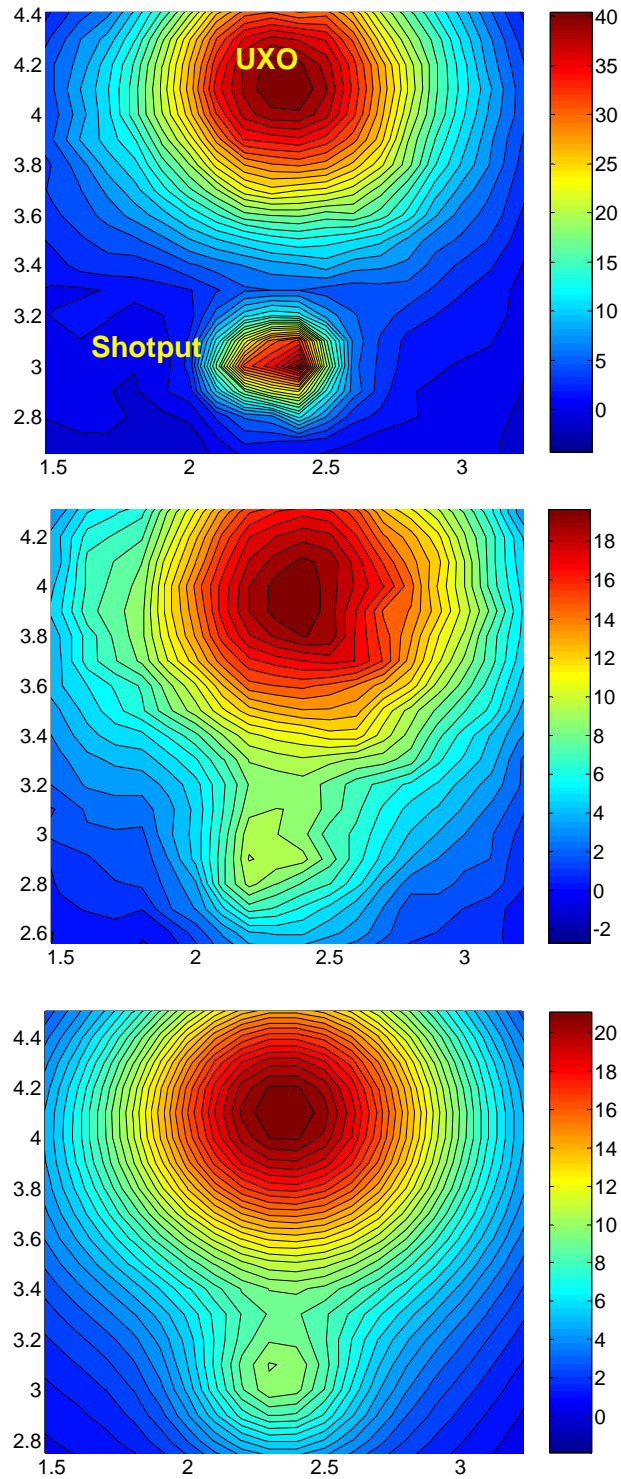
Figure 19. Single shotput clutter case with 105 mm projectile buried vertical nose down initially at 73 cm from sensor to tail. Top: Data at initial sensor distance. Middle: Data at 23 cm higher sensor distance from both targets. Bottom: Computational continuation 23 upwards of data in top plot.

- -

An example with two clutter items (Figure 20) shows even more pronounced reduction of clutter signals with increased distance from the sensor. The clutter arrangement includes the right-most two shotputs in Figure 14, bottom. Despite the fact that the identical clutter items were both the same distance below the sensor platform, the magnitude of their signals is somewhat different because of their differing relations to the survey lines and sensor paths. The shotput near the bottom of each plot was located somewhere between the sensor lines such that interpolation between the lines could not catch its true peak. In any case, in the upper plots the greatest clutter signal magnitude is on the order of 50% greater than that of the UXO. At the greater sensor distance (bottom plots) the situation is reversed, with the UXO signal now roughly twice that of the clutter. Note again that, in addition to reproducing this effect, upward continuation has also cleaned up the random noise that actually increases in the physical data taken from greater distance.

Pursuing this, we use the algorithm to continue the data to greater sensor distances than were possible to produce in the field. This exploits the greatest benefits of upward continuation. Figure 21 shows continuation of the original data to two higher levels, in the course of which the two clutter signals fade increasingly. Ultimately it is clear that most of the signal is due to the target of interest, the UXO (Figure 21, bottom).
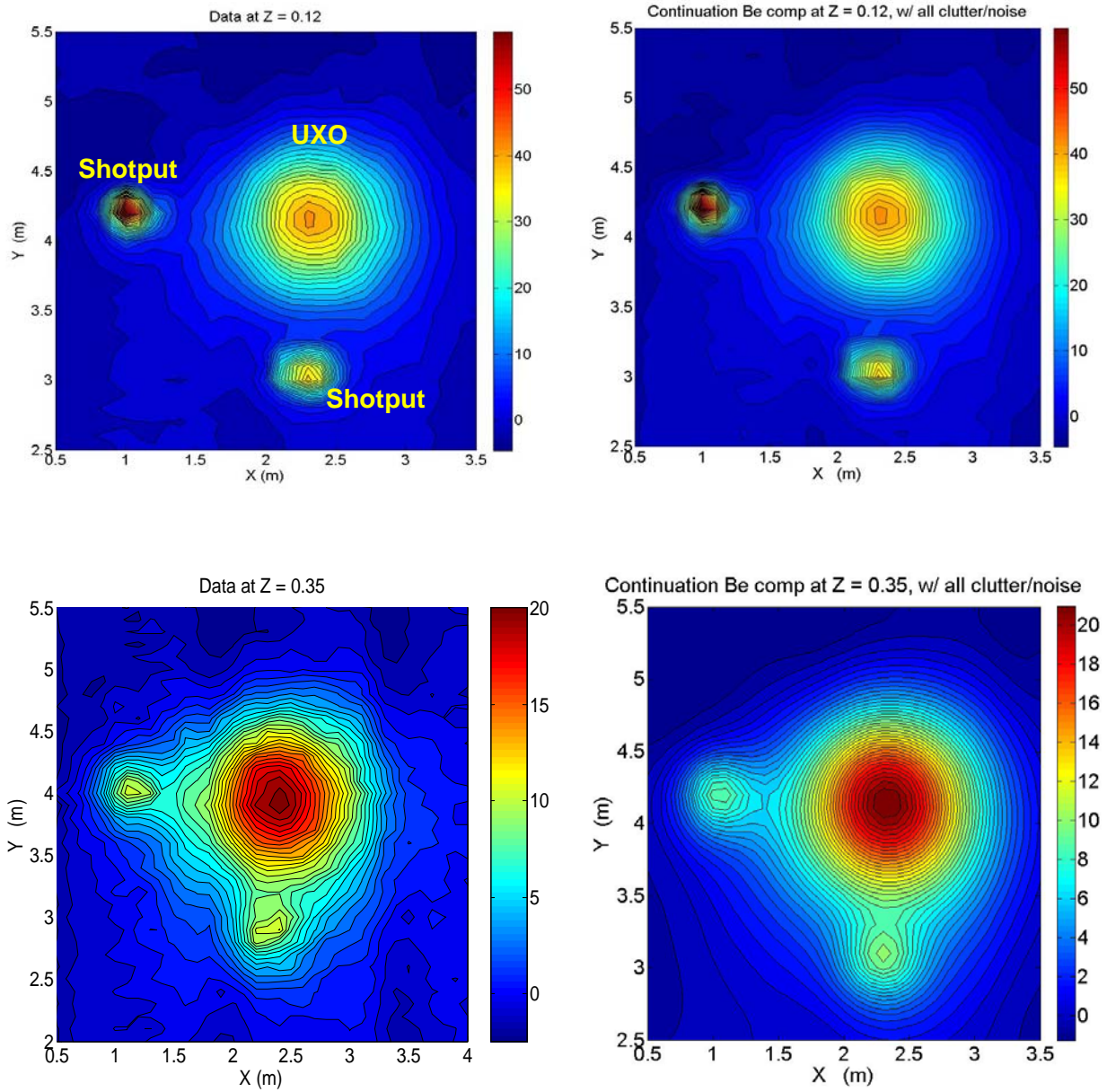
Figure 20. Case with clutter produced by two shotputs and 105 mm projectile at center. Left: data. Right: Continuation results. Top: Initial elevation. Bottom: 23 cm greater distance to sensor for all targets.
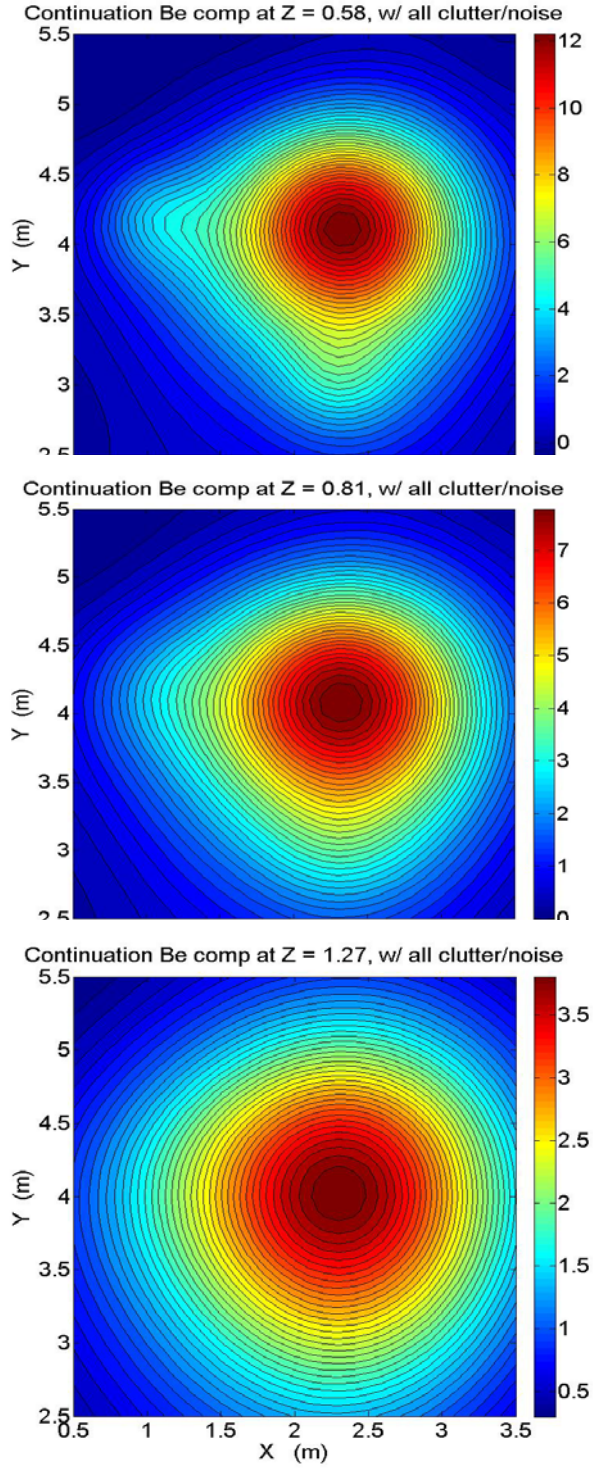
Figure 21. Computed signals for 105 mm UXO plus two surface clutter items, with data continued beyond the 35 cm elevation of the previous figure, to 58 cm, 81 cm, and 127 cm (top, middle, bottom).

Before proceeding to the next field test, we return briefly to a modeling exercise to assess better what one might expect in more problematical cases. The cases above treat only instances in which distinct clutter appears at positions offset from the UXO response. While this was useful for ascertaining the relative strengths of the clutter and target signals, it does not treat the situation of greater interest, namely, when the clutter is superposed intrusively on the UXO signal. Figure 22 shows one rendering of field data for a case in which the clutter was placed directly above the center point of an inclined UXO. The combination of target inclination and the applicable $\hat{\mathbf{B}}_e$ at APG causes the clutter to appear off center on the target signal distribution. In any case, the clutter produces an impressive spike on the smoother UXO response. Can the method here really help in this kind of situation?
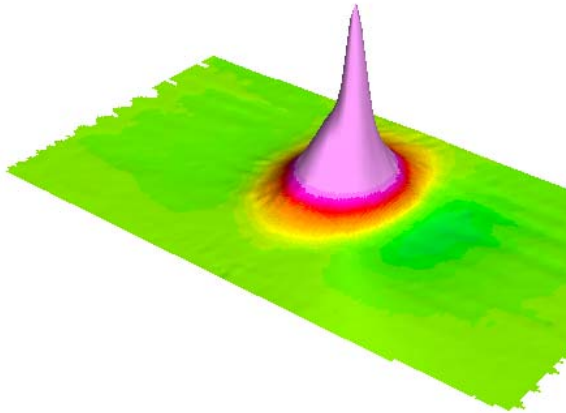
Figure 22. Field data from a case in which a shotput is placed on the surface above a buried 105 mm projectile inclined at 45°.

For visual simplicity we assume in a simulation that $\hat{\mathbf{B}}_e = -\hat{\mathbf{z}}$ and the target is a vertical dipole which by itself will produce a radially symmetric signal. A horizontally offset clutter item with 5% of the target's dipole moment is placed at 6 cm depth, vs 60 cm for the UXO. This produces a bump on the target signal on the measurement plane S_m at 20 cm elevation (Figure 23, top) comparable to that in field data in Figure 22. At a height of 1.2 m the continuation signal catches the main character of the signal sought from the target alone. It has tracked its decline in magnitude from ~ 0.3 to ~ 0.03, with similar spread of the overall pattern. These results suggest that even strong clutter directly within the main target response can be reduced by our method. Bolstered by this simulation result, we proceed to a comparable case in the field.
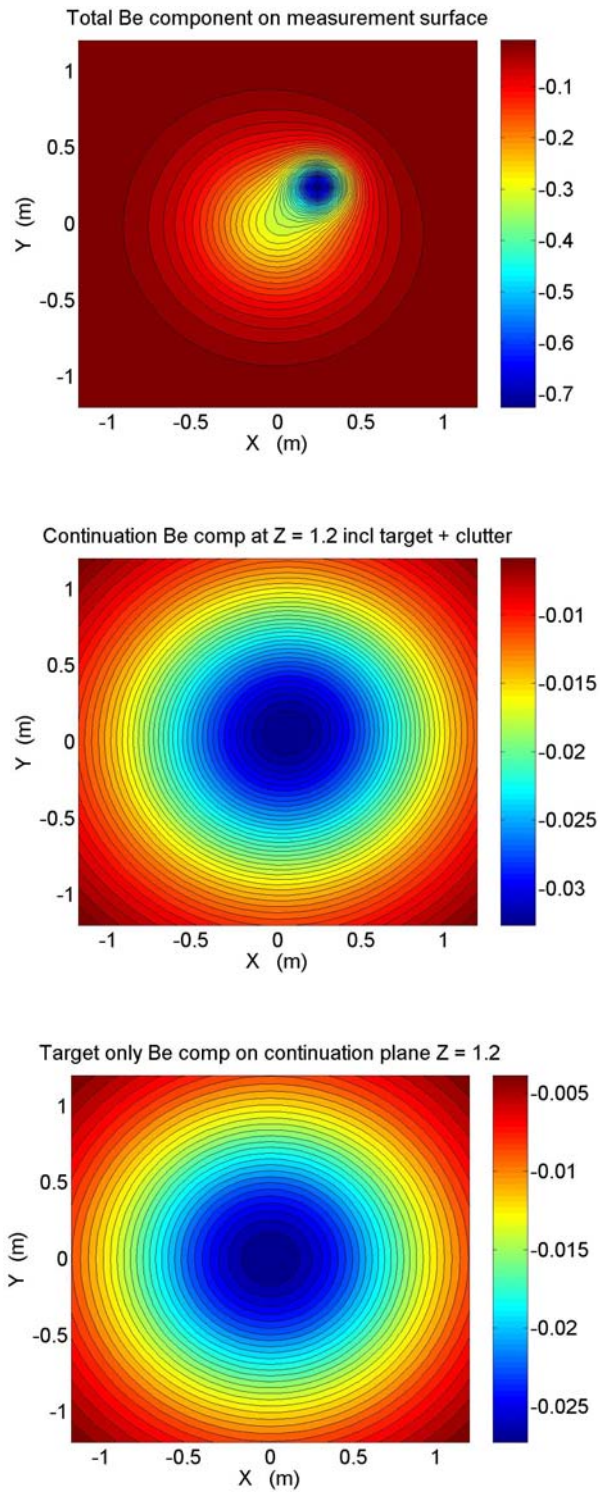
Figure 23. Simulation case in which a clutter item is located such that its signal intrudes upon that of the UXO. Top: Data plane S_0 at $Zm = 0.2$ m with prominent clutter. Middle: Continuation signal from UXO plus clutter at $Z = 1.2$ m. Bottom: Target only signal, also at $Z = 1.2$ m.

Figure 24 shows results for a case involving a 105 mm projectile buried at a 45 deg inclination, with and without a shotput placed directly above. The addition of the shotput (upper right) to the scenario with only the UXO (upper left) produces a spike in the signal about two and a half times the signal magnitude from the UXO alone. The clutter item changes the signal distribution very markedly. However upward continuation of the data including the obtrusive clutter catches the main character of data we should expect at elevation from the UXO alone.

no shotput   with shotput
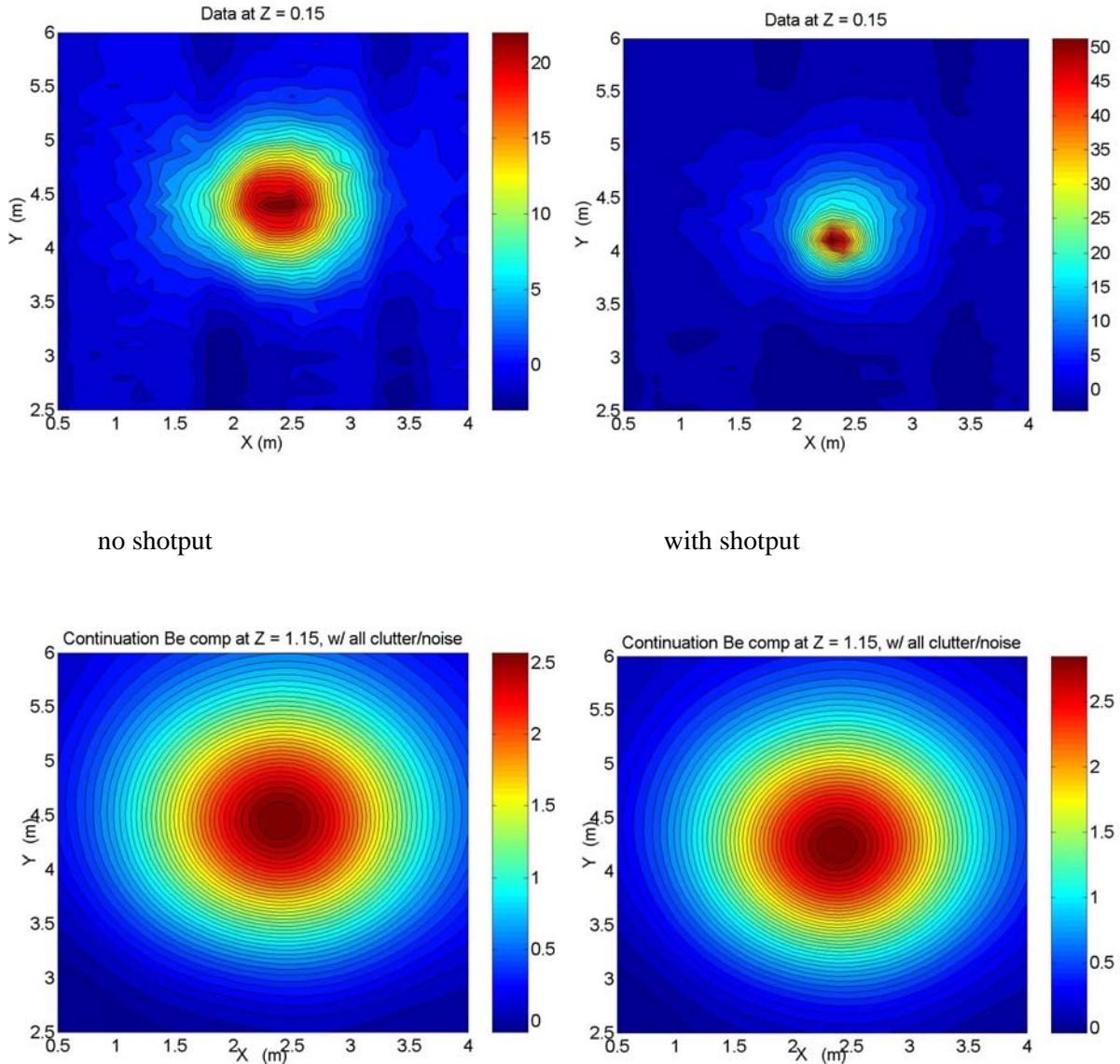
Figure 24. Field case with 105 mm at 45 deg inclination and $d = -81.5$ cm, with and without shotput directly above. Top: Data on S_0 at 15 cm elevation. Bottom: Continuation calculations for 1 m higher elevation. Left: UXO alone (no shotput). Right: UXO with shotput above it.

4. The Downward Computation Issue

Downward continuation can mean different things to different people; however, all employing it seek in some way to extend above-surface information to infer the subsurface situation. At least from the point of view of consistency in terminology, the most logical meaning would be use of [above-]surface information to calculate subsurface fields of the same kind that were measured. Additionally, we take the term to mean here true continuation involving fully multi-static data, as opposed to projection to some other level of mono-static data: A single, spatially widespread response field is continued. In this view, detailed surface information is, after all, a kind of boundary condition. One can consider the boundary to delimit either an upper or lower half space. While here the field values are not calculated directly using integral or differential equations, the computational framework is arguably equivalent via the intermediate device of equivalent sources. Information at one level is used to solve for distributions of equivalent sources over deeper surfaces. This implies directly a distribution of the field component normal to the deeper surface, and thence all field components. In any case, by computing source distributions over deeper and deeper surfaces one might seek to find a depth where the source concentration is greatest, taking this to be the location of the object of interest. The motivation can be just to locate the target, or to infer some of its properties by examining the focal source distribution.

Aside from details of computational strategy and their various pro's and con's, all downward continuation strategies are challenged by the same issues: 1) Separation of the data plane and the deeper source (continuation) plane tends to produce ill-conditioned systems; and 2) proceeding deeper with the calculations is inherently a clutter/noise amplifying process. Under the conditions with which one must contend here using total field magnetometers, the source plane must be displaced to some position below the data plane even in upward continuation. Thus ill-conditioning is a potential issue there as well, even in the absence of any more ambitious lowering of the source plane. The second issue is limited to downward continuation. The results above show smoothing of surface noise as the signal is continued upward. It is not surprising then that, proceeding in the opposite direction, one should confront the opposite phenomenon.

To make the problem palpable, the following example considers noiseless data with a single source of signal at a specified depth (Z = -20 cm). There is no loss of generality in that noise caused by perturbations of some kind at the surface would simply serve as a broader distribution particular sources, at a shallower depth. Studying the effects of a single source will suffice to make the point. Also, deleting noise beyond what is caused by the discreet object avoids confounding the noise/clutter amplification issue with ill-conditioning's similar effects. For simplicity consider the earth's field to be vertical, and the dipole moment of the object at 20 cm depth to be $\mathbf{m} = [0\ 0\ 1]$. Using data from a plane S_m that is 20 cm above the "ground surface"(S_0 at Zq = 0), with data and source points on a grid with 10 cm spacing, one obtains the source distribution in Figure 25, top. Lowering S_0 to -20 cm, i.e. to the same level as the concentrated dipole source, produces the middle plot. This is as concentrated a source distribution as the particular computational parameters will permit.

The point of this exercise is apparent in the bottom plot of Figure 25. Here S_0 has been lowered another 20 cm to Zq = -40 cm. The computed values oscillate wildly and spread out spatially. Both the limits of the oscillations and any smoothing of the distribution comprise values that are orders of magnitude higher than the most concentrated sources at the depth of the object (middle plot). The system is demonstrating that much more in the way of sources is required at more distant regions to produce the effect of the nearer object. Now, if the only purpose were to isolate the object, one could perform these computations but then simply discard the results in Figure 25, bottom, satisfied that the middle plot represented something of a "focal" point. However the problem is clear if one considers that the hypothetical object at 20 cm depth might be simply a piece of clutter and the object of real interest deeper. Clearly the kind of source distribution in Figure 25, bottom, would obscure any more reasonable distribution associated with a discrete target at comparable or greater depth. In the course of downward continuation, the computational system will in fact tend to spread and amplify greatly any near-surface perturbations or effective sources in the data, independent of (similar looking) ill-conditioning effects.

These results argue strongly against pursuing downward continuation. At the same time, one can apply special measures that may help, and which in any case are likely to be required by ill-conditioning, to which we pass in the next section.
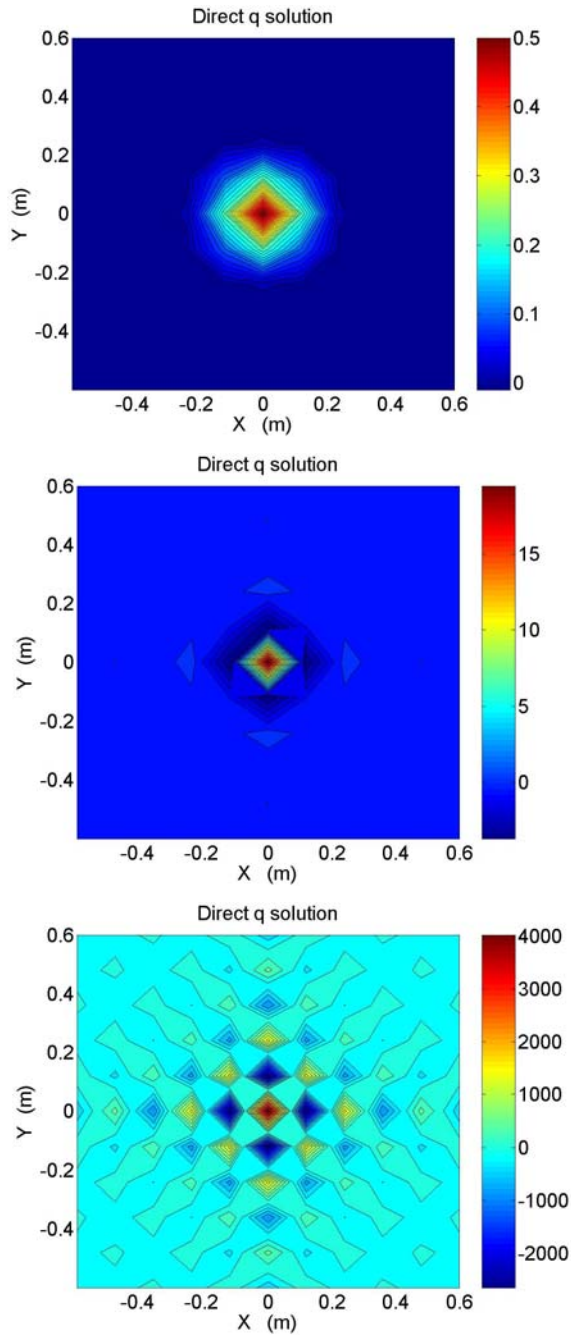
Figure 25. Solutions for q_B obtained in a hypothetical example when the target is at 20 cm depth. The location of the source plane S_0 is at depths Zq = 0 (top), Zq = -20 cm (middle), and Zq = -40 cm (bottom).

5. Computational Control of Solutions for Distributions of Sources at Depth

5.1. *Uniqueness and Invertability for Sources*

For both the upward and downward continuation strategies pursued here, one needs to compute planar distributions of sources at some level below that where data were obtained. Especially if one wishes to gain some view of a source concentration around the actual target location, it is tempting just to measure the secondary field over a surface at a chosen elevation and then, using the equivalent of (12), to solve for a distribution of sources over an entire volume below. Ideally the distribution of equivalent sources would concentrate wherever a significant physical source was located. However this problem is inherently ill-posed. To see this, consider a simple case in which the source is a unit magnitude point charge at the origin. On the basis of (8) only a radial field component is produced, namely $B_r = 1/4\pi r^2$. Using the formulation above but applied to curved instead of flat surface, one can produce this field outside a spherical surface with some radius r_1 by assuming a distribution of equivalent magnetic charge over the surface of the sphere.

$$q_B\left(r'=r_1\right) = \frac{1}{2\pi r_1^2} \quad \rightarrow \quad B_r\left(r > r_1\right) = \frac{1}{4\pi r^2} \tag{19}$$

By the same reasoning, however, one can also produce the same field from a distribution of charges over a different sphere about the origin, e.g. with radius $r_2 > r_1$.

$$q_B\left(r'=r_2\right) = \frac{1}{2\pi r_2^2} \quad \rightarrow \quad B_r\left(r > r_2\right) = \frac{1}{4\pi r^2} \tag{20}$$

Thus at any $r > r_2 > r_1$, both distributions of sources produce exactly the same field.

If the sources are distributed over a surface instead of a volume, however, a unique set of sources is implied by the fields observed over that surface (see (10) and discussion surrounding it). One may specify sources, point by point, just based on direct correspondence to field boundary conditions over the surface. Our computations are a bit more indirect than point by point correspondence between $2H_z$ and q_B in that the observed field values on S_m are offset spatially from the surface S_0 on which the sources lies. However the same logic prevails: a given field boundary condition on S_0 will produce specific field values in the region above it. Any alteration of those boundary values will inevitably produce a change in field values somewhere in the region above, i.e. where S_m is. Therefore only a single boundary condition on S_0 and single corresponding source distribution on it will produce interior field values that match those observed over the entirety of S_m.

We take the gist of the discussion above to imply that one may assume that a unique set of sources q_B is implied over a plane by our observations of some component of the field over S_m. In fact, some issues of invertability and uniqueness, necessity and sufficiency of conditions are not addressed in complete depth in the foregoing discussion. While reserving full pursuit of those issues for follow-on work, we take the reasoning above together with computational experience to provide confidence that the numerical system (11)-(12) is inherently invertible.

5.2.   Ill-conditioning and Its Control

Unfortunately, while this is reassuring, we have not entirely escaped the issue of ill-posedness in the form of its numerical first cousin, ill-conditioning. The problem is that, as the surface S_0 is located at increasingly greater depths relative to the observed data, the system becomes increasingly ill-conditioned. To understand this, consider the following relation

$$\begin{bmatrix} 2 & 0 \\ 0 & 10^{-4} \end{bmatrix} \begin{Bmatrix} H_{ax}^{PR} \\ H_{tr}^{PR} \end{Bmatrix} = \begin{Bmatrix} S_{ax} \\ S_{tr} \end{Bmatrix} \tag{21}$$

This might apply to the EMI response of some very elongated object, when the coordinate system is aligned with the axial and transverse axes of the object. The axial and transverse sensor signals

on the right hand side are related by the matrix diagonal values to the impinging primary fields along the those same axes. Suppose we observed the signals on the right hand side and wished to infer the primary fields hitting the target that had produced them. In this instance, with real data, the problem would be quite difficult even though the matrix is immediately invertible by inspection. This is because, in our example, the transverse response is inherently so weak. Given comparable values of H_{ax}^{PR} and H_{tr}^{PR}, the transverse signal S_{tr} will be much weaker than S_{ax}. S_{tr} may likely be predominately noise. This will produce a greatly distorted value of H_{tr}^{PR} when S_{tr} is divided by 10^{-4}.

Basically the matrix in (21), while perfectly legitimate and consistent, is telling us not to try to solve for the second unknown because its effects are much too weakly represented in the system to be clearly distinguishable. The difficulty is also evident if one simply rotates the coordinate system so that the matrix becomes

$$A = \begin{bmatrix} 1.0 & 0.9999 \\ 0.9999 & 1.0 \end{bmatrix} \tag{22}$$

Here the pathological nature of the system is clear in another way: the original system is equivalent to having two nearly identical equations, a bad prospect for solving for two unknowns. For all practical purposes, the system really only contains one independent statement.

The degree of ill-conditioning in a system is typically quantified in terms of condition number C, which equals the magnitude of the ratio of the largest to the smallest eigenvalues of the matrix. In this example $C = 2 \times 10^4$, as the matrix in (21) in fact contains the eigenvalues on the diagonal. A rule of thumb is that a condition number on the order of 10^n will amplify unacceptably noise that is on the order of 10^{-n} or larger relative to significant values of the data. That is, for stable, accurate solutions, one requires an SNR at least on the order of C, ideally an order of magnitude better. This is a challenging requirement. For problems such as those considered here, C values greater than 100 appear very easily, whereas an SNR greater than 100 is normally very hard to come by.

Referring back to Figure 3, one can see how ill-conditioning may arise in applying (12) here. If two source points on S_0 are too close together, they will produce very nearly the same

- -

equation in the governing matrix: each has nearly the same influence on the data. For a given separation of source points, moving S_0 further away from S_m has the same effect as moving the source point closer together in terms of our ability to distinguish their influence. By analogy, if each source in a group of such source points emits a glow of light, when they are moved far enough away from the observing surface they will simply appear as a single blob of glow with no distinguishable effects attributable to the individual sources. Similarly, placing the observation points on S_m too close together will have the same effect. Overall, trying to increase resolution by using finer divisions on either S_0 or S_m will exacerbate ill-conditioning in a highly nonlinear fashion.

In the field cases considered in this report, care was taken in terms of separation of S_0, S_m, source points, and observation points so that ill-conditioning was not a problem. However, only small changes in these spacings would be required to produce substantially worse conditioning. Overall, in general application of the methods of upward continuation proposed here over any variety of situations, the appearance of ill-conditioning problems is virtually inevitable. Further, if one attempts to move the S_0 source plane farther and farther away from the data plane - proposed here for isolating physical sources - problematical ill-conditioning is to be expected. Figure 11 illustrates a simulation case in which spacings that were not at all extreme produced substantial noise amplification via ill-conditioning.

In computational practice the matrices to be dealt with do not normally present themselves in such a convenient form as that in (21). While the actual matrices from (12) are full, as in (22), their insufficiency is much less evident. They are much larger; the full matrix system is not readily seen as a geometrical rotation of a clearer system; and problematical components are not readily visible as being too similar to one another. At the same time, generalized "rotations" may be applied so that the system is translated into an eigenvalue-eigenvector basis. The material below pursues ways to use eigenvector and other decompositions of the system to restrict the solution to well-supported components.

The overall strategy here of evading ill-conditioning can be outlined as follows. Consider a linear system

$$L[q] \;=\; H \tag{23}$$

- -

in which *L* is some linear operator, e.g. the matrix implied by (12). *H* constitutes the data and we are to solve for *q*. Re-express the quantities *H* and *q* so that they are expressed by series containing a new basis.

$$L\left[\sum_j q_j \phi_j(\mathbf{r})\right] = \sum_m H_m \phi_m(\mathbf{r}) \tag{24}$$

The functions ϕ_m and ϕ_j are members of the new basis and H_m and q_j are coefficients. The bases need not be the same for both *H* and *q* though in what follows they will always be so.

Multiplying (24) by any one basis function ϕ_i and integrating (taking a suitably defined scalar product <...>) produces the relation

$$\sum_j q_j \left\langle \phi_i L\left[\phi_j\right]\right\rangle = \sum_m H_m \left\langle \phi_i \phi_m \right\rangle \tag{25}$$

and one can now solve for the coefficients q_j. The change of basis is selected in such a way that the system can be truncated sensibly, altogether deleting equations and corresponding (transformed) unknowns that have weak support. The basis functions are constructed so that they are independent and, ideally, orthogonal under the scalar product definition, i.e.

$$\left\langle \phi_i \phi_m \right\rangle = \delta_{im} \tag{26}$$

where δ_{ij} is the Kronecker delta. Strong independence in the form of the orthogonality is advantageous in a number of ways. First, we noted above that when source or observation points are physically close to one another so that their contributions to the system are similar, ill-conditioning will tend to result. Hence here we seek a mathematical space in which to operate in which the known and unknown quantities are associated with maximally independent influences in the system. Secondly, (26) simplifies computations greatly. In matrix terms, $\left\langle \phi_i \phi_m \right\rangle$ just becomes a diagonal matrix and therefore no onerous manipulations are required to invert the system. Lastly but perhaps most important, one can examine the elements on the diagonal matrix

- -

$\langle \phi_i \phi_m \rangle$ to see directly and easily which of them are weak, hence where to truncate the series in (25).

In what follows we examine two approaches to transforming the system into a form in which weak elements are discernible and readily subject to elimination, namely use of eigenvector bases and of sinusoidal bases.

5.2.1. Eigenvector Decomposition and Exclusion of Weak Eigenvalues

The eigenvector decomposition approach to dealing with ill-conditioning has been recognized in a number of numerical applications, e.g. [10]. One proceeds as above, using (12) to produce an algebraic equation of the form

$$A q \;=\; H \tag{27}$$

where H is a vector of the data and the vector q contains the point sources to be obtained. The transformations operate directly on the already discretized system, not on the original continuous integral relation (11).

The matrix A is decomposed in terms of its eigenvectors and eigenvalues as

$$A \;=\; Q \Lambda Q^{\mathrm{T}} \tag{28}$$

where Q contains the normalized eigenvectors and Λ is a diagonal matrix of eigenvalues. While similar formulations may be produced for rectangular systems of equations, in all examples here square matrices are used so we remain with the form in (28). By virtue of their mutual orthogonality property, the normalized eigenvectors form a matrix with the property that its transverse is its inverse:

$$Q Q^{\mathrm{T}} \;=\; I \tag{29}$$

- -

The quantities H and q can be re-expressed in an eigenvector basis as

$$
\begin{aligned}
H &= Q\eta \\
q &= Q\nu
\end{aligned}
$$

(30)

Combining these equations produces an algebraic system in terms of quantities in the transformed space, i.e. in the new variables $\eta = Q^{\mathrm{T}}H$, $\nu = Q^{\mathrm{T}}q$.

$$
\eta = \Lambda\nu
$$

(31)

The inversion of this system is immediate, as the matrix Λ is diagonal. This set of steps is the equivalent of starting with the matrix in (22), for example, and transforming it to that in (21). Ultimately, source values q can be obtained from the solution for the transformed variable ν via (30).

The point of these manipulations is that, as in our treatment of (21), one can discern readily in the transformed system what equations are too weak to merit inclusion in the total system. Equations in (31) containing eigenvalues that are smaller than some cutoff α relative to the maximum (absolute value) $\lambda_{\max}$ are discarded. That is, the complete solution ν is approximated by $\tilde{\nu}$,

$$
\tilde{\nu}_i = \begin{cases} \dfrac{\eta_i}{\lambda_i}, & \lambda_i/\lambda_{\max} > \alpha \\ 0, & \lambda_i/\lambda_{\max} \le \alpha \end{cases}
$$

(32)

from which

$$
q \approx q_{\mathrm{m}} = Q\tilde{\nu}
$$

(33)

Note that this produces the same number of elements in q as before (n), but simply using a subset of m of the complete set of n eigenvectors. Using the complete set of eigenvectors ($m = n$) will produce strict equality between q and q_{m}.

- -

To investigate and to illustrate eigenvector decomposition we pursue some simple 1-D examples. The solution is taken to be $q = \sin(\pi n / 33)$ and a 100 x 100 symmetric matrix A is produced using a random number generator, resulting in $C \sim 5 \times 10^3$. H is obtained from Aq. Error in the data H is produced by adding random white noise over a band of values [-b, b], where

$$RelNoiseMag = \left| \frac{2b}{H_{max}} \right| = 0.05 \tag{34}$$

This combination of C and $RelNoiseMag$ will normally produce an unacceptably distorted solution: the SNR (loosely defined) is on the order of 20, while something on the order of 5000 or better is needed. Figure 26 shows the right hand side (data, H) obtained from the A and q that have been specified. Note that the noise is considerably less than is typically the case in real field data.
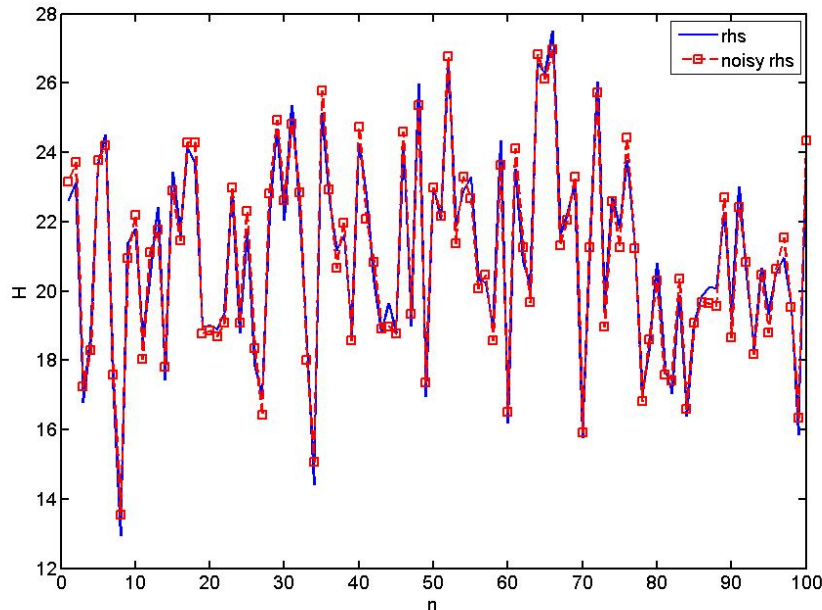

Figure 26. Right hand side H in (27), with and without noise at $RelNoiseMag = 5\%$.

Without added noise, the precision of the data H (roundoff error in the computer) still securely places its SNR above that required by the condition number. Hence the noise free

- -

solution of (27), not shown, is extremely accurate, with no graphically visible distortions. At the other extreme, direct solution of the system with added noise at the indicated level produces q values that are predominately just amplified noise. If one retains the noise-free data and truncates the eigen-system, using a cutoff of $\alpha = 10^{-2}$ with resulting $m/n = 85/100$, the solution in Figure 27, top, results. The solution visibly follows the actual (exact) solution. However, truncating the eigen-system at a "safe" level discards enough meaningful information so that, in translation back from ν to q, the deletions cause lumps and bumps. This highlights a basic problem in the eigen-system truncation approach. Namely, the nature of different portions of the information in the eigen-system may not mean that retaining values above a certain level of significance will translate into values above that level of significance in the original space.

Figure 27, bottom, shows the solution obtained by the same eigen-system truncation but using the noisy data in Figure 26. There are discernible differences between the solution from the noise-free and noisy data. However these are slight. The eigen-system truncation has indeed restrained the influence of noise in the data to a minor factor, although the truncation itself has still left some distortions.
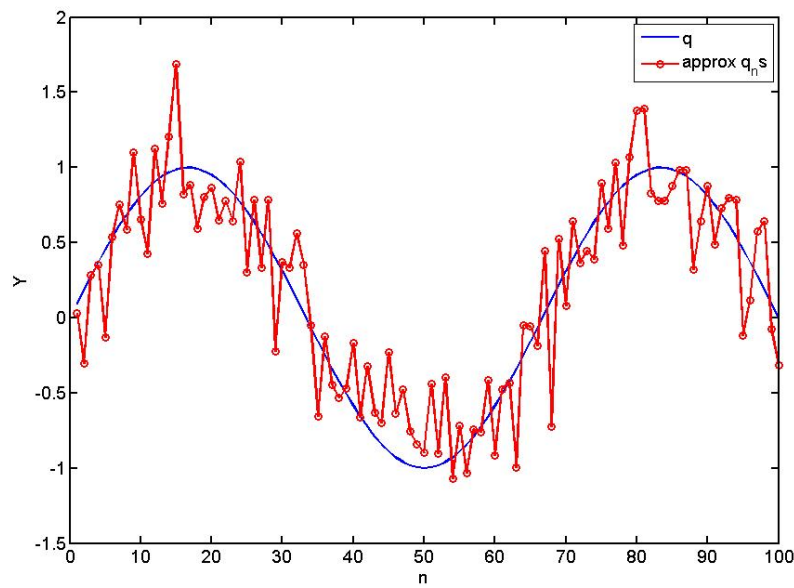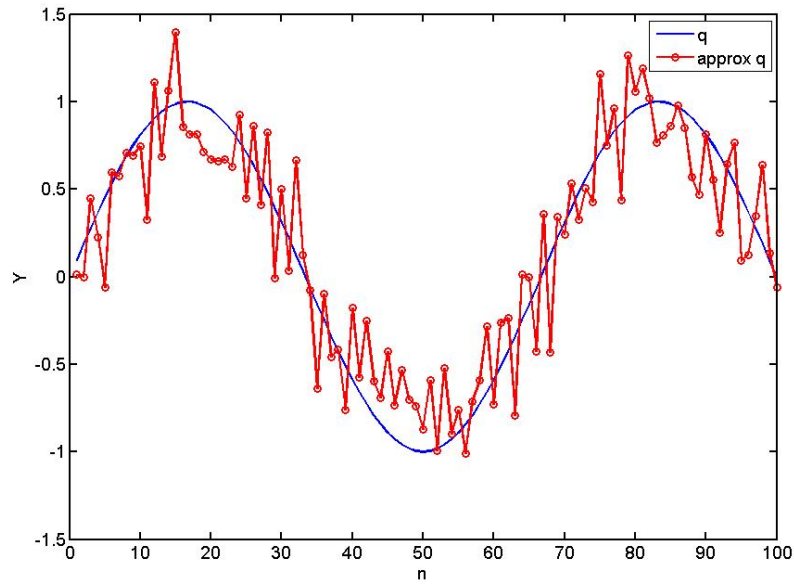
Figure 27. Top: truncated eigen-solution without noise added to data. Bottom: same, but
when noise was added to the data.

5.2.2. Fourier Decomposition and Exclusion of Insufficiently Supported Spatial Frequencies

The formulation in this approach operates directly on the continuous variables and integral expression (11), producing an alternative discrete system which is readily truncated to advantage. It exploits relations and strategies outlined in [2]. Essentially, the system is translated into the (spatial) frequency domain, in terms of spatial 2-D Fourier transforms of both the data and of the source distribution. This allows one to solve for q_B coefficients, again without in fact inverting any matrices, truncating the system at spatial wave numbers beyond which contributions are negligible. Note that, without treatment, the solution noise that "slips through" the linear operator from the data tends to correspond to high spatial frequencies. In Figure 11, the very substantial distortions in the solution appear in the form of values oscillating between relatively large positive and negative values between neighboring points. From one point of view, this is a relatively benign form of noise in that it tends to integrate out when one uses (11) to calculate field values at some elevation. The (numerically expressed) integral has something of a "blind spot" for information at this frequency. This is convenient for upward continuation. However, when one proceeds in the inverse direction, the integral and its numerical equivalent are not good at restricting data noise of this wavelength from assuming an arbitrary large value in the solution. Our strategy will be to recast the system in the frequency domain and then to forcibly truncate the participation of frequencies higher than the system will readily support accurately.

To proceed, express q_B as

$$q_B\left(\mathbf{r}'\right) \; = \; \sum_{m=1}^{M}\sum_{n=1}^{N} \sigma_{m,n} e^{ik_m x'} e^{ik_n y'} \tag{35}$$

Equation (12) becomes

$$b_e\left(\mathbf{r}\right) \; = \; \sum_{m,n} \sigma_{m,n} \int_{S_0} dS' \frac{e^{ik_m x'} e^{ik_n y'}\,\hat{\mathbf{B}}_e \cdot \left(\left(x - x'\right)\hat{\mathbf{x}} + \left(y - y'\right)\hat{\mathbf{y}} + d\,\hat{\mathbf{z}}\right)}{4\pi\left[\left(x - x'\right)^2 + \left(y - y'\right)^2 + d^2\right]^{3/2}} \tag{36}$$

where, conveniently, we benefit from the fact that $(z - z')$ is uniformly equal to some depth d (both data and sources are assumed to be located on planes of constant z). In principle, the expression in (35) could be written as an integral of continuous quantities rather than a finite sum of discrete terms. In that case, *any* two different k values, say, k_i and k_j will be associated with basis functions that fulfill our orthogonality requirement that

$$\int_{-\infty}^{\infty} dx' \, e^{i(k_i - k_j)x'} = \delta_{ij} \tag{37}$$

so that (26) applies. In numerical practice, the integration is over some suitable finite interval and a corresponding finite selection of k values is used, as in the summation (35). For example, driven either by the need for a certain minimum domain size or a certain spacing of wavenumbers, one might pick the domain size L with $k_m = 2\pi m/L$. Matlab, in which language system the computations here were performed, automatically applies a k selection of this sort in its FFTs and IFFTs so that a discrete form of (37) holds exactly.

With a change of variables

$$u' = x - x', \quad v' = y - y' \tag{38}$$

(36) becomes

$$b_e(\mathbf{r}) = \sum_{m,n} \sigma_{m,n} e^{ik_m x} e^{ik_n y} \int_{u',v'=-\infty}^{\infty} dS' \frac{e^{-ik_m u'} e^{-ik_n v'} \hat{\mathbf{B}}_e \cdot (u'\hat{\mathbf{x}} + v'\hat{\mathbf{y}} + d\,\hat{\mathbf{z}})}{4\pi \left[(u')^2 + (v')^2 + d^2 \right]^{3/2}}$$

$$\tag{39}$$

$$= \sum_{m,n} \sigma_{m,n} e^{ik_m x} e^{ik_n y} V(k_m, k_n)$$

where V need only be calculated once for each d. It is basically just a weighted FT of the Green function for b_e, referred to the origin. A significant attraction of this approach is that all $\mathbf{r}$ dependence of b_e (beyond d) is contained in the exponentials $e^{ik_m x} e^{ik_n y}$ outside the integral. Values of V for each d can simply be stored and used for arbitrary $\mathbf{r}$ as required.

- -

The remaining exponentials in (39) can be integrated out if one expresses b_e itself as

$$b_e(\mathbf{r}) = \sum_{\text{m}',\text{n}'} p_{\text{m}',\text{n}'} e^{ik_{\text{m}'}x} e^{ik_{\text{n}'}y} \tag{40}$$

for the same set of wavenumbers as were used for q_B. The coefficients $p_{\text{m}',\text{n}'}$ are simply obtained from the FT of the data. To conclude, substitute (40) into (39), multiply by $e^{-ik_i x} e^{-ik_j y}$ and integrate (x,y) each over $(-\infty,\infty)$ or over the aforementioned suitable interval, to obtain

$$p_{i,j} = \sigma_{i,j} V(k_i,k_j) \tag{41}$$

for each (i,j). As in the previous approach, all quantities are now scalars and no matrix solution is required.

The truncation is accomplished by retaining only spatial frequencies that contribute to the solution securely:

$$\sigma_{i,j} = \begin{cases} \dfrac{p_{i,j}}{V(k_i,k_j)}, & V/V_{\text{max}} > \alpha \\ 0, & V/V_{\text{max}} \leq \alpha \end{cases} \tag{42}$$

While geographically applicable $\hat{\mathbf{B}}_e$ may make the k dependence of V non-monotonic, the system in (42) succeeds in filtering out all frequencies with insufficient support, whether high or low. In any case, the nature of Fourier decomposition is such that k values above some level will inevitably contribute little to both the data and the solution, whatever the pattern of dependence on lower k values. High frequency noise influences will be filtered out.

Equation (41) indicates that individual Fourier components of the data are only associated with individual, corresponding Fourier components of the source distribution. This prompts the question of whether the necessary truncation of $\mathbf{k}$ space for V will be sufficient to define q_B well.

- -

This relates in part to the frequency resolution level that is inherent in the integral operator. Probably of greater concern is the specific frequency content of the data, i.e. whether the range of significantly contributing wavenumbers in the data is sufficient for the requirements of $\sigma_{i,j}$. The spatial distribution of the data b_e will in general be broader than that of q_B as deeper and deeper S_0 are considered and q_B becomes increasingly concentrated. Higher and higher $\mathbf{k}$ will be required for q_B, which may not be supported by b_e, i.e. the corresponding $p_{i,j}$ may be essentially noise.

To explore these questions and to test the frequency truncation approach overall, we begin with a simplified simulation case in which the earth's field ($\hat{\mathbf{B}}_e$) is vertical and the responding subsurface body is a vertical dipole. This produces symmetrical signal patterns that are easy to assess visually. With the target at $d = -0.5$ m and $\alpha = 0.01$, the solutions in Figure 28 result. The upper right plot in the figure shows what perfect, noise-free data would look like. The two plots of the noisy data reconstructed from the truncated q_B solutions (middle and bottom right) illustrate the level of clutter in the noisy data. Without either eigen-system or frequency value truncation, a direct solution for q contains very large oscillations between neighboring points (upper left plot). In contrast, both of the truncated systems produce tolerable renderings of an equivalent source distribution half a meter above the actual, infinitely concentrated physical source (middle and bottom left plots).

Lowering the source place S_0 in order to cause the q pattern to focus on the physical source location produces the results in Figure 29. The truncated solutions succeed at least in the sense that they remain coherent, with noise suppressed. By contrast, a direct q solution (no truncation, not shown) for $Zq = -0.5$ m covers whole plane, oscillating between $\pm 10^{10}$. However neither of the truncated solutions focuses notably on the infinitesimal physical source. As Zq drops below zero ("ground surface") and the condition number rises exponentially, the eigen-system truncation allows fewer and fewer eigenvectors to participate (m/n decreases, see plot headers). Similarly, the resolution of the frequency truncation system is also limited, either because of the limited range of the spectrum of the data or of the (numerical) integral operator, or both. The finite focusing of the truncated solutions in the figures is summed up in Table 1. These results suggest that, while both methods stabilize the solution impressively in the face of enormous condition numbers, neither is likely to be useful for focusing on subsurface source locations.
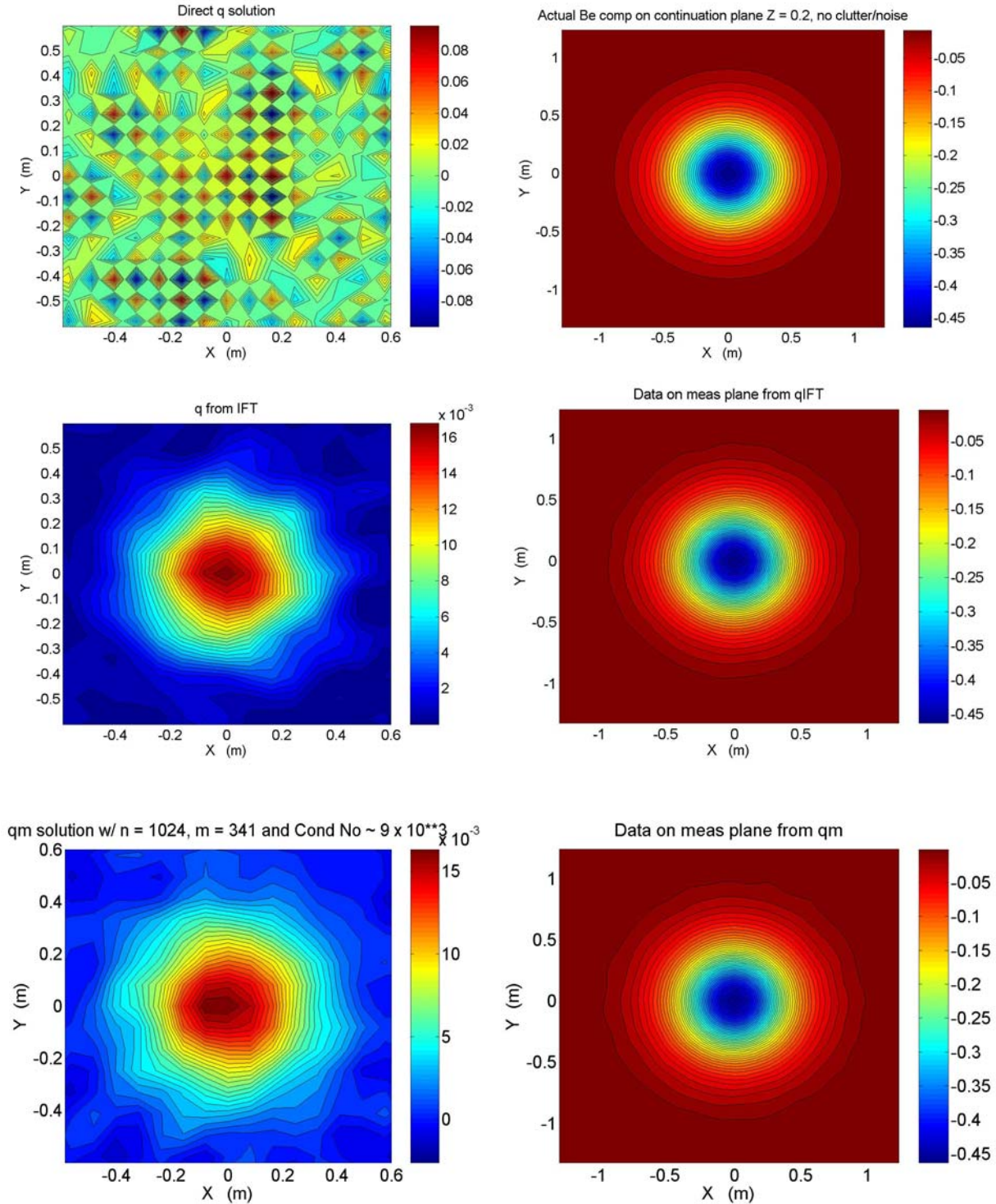
Figure 28. For data taken 20 cm above the surface, with the source plane S_0 on the ground surface ($Zq = 0$ cm). Left: Direct q solution (top); that from the truncated FT (middle); and that from the truncated eigen-system (bottom). Right: Data without added noise (top); noisy data reconstructed from truncated FT source solution (middle); same, reconstructed from truncated eigen-system (bottom).
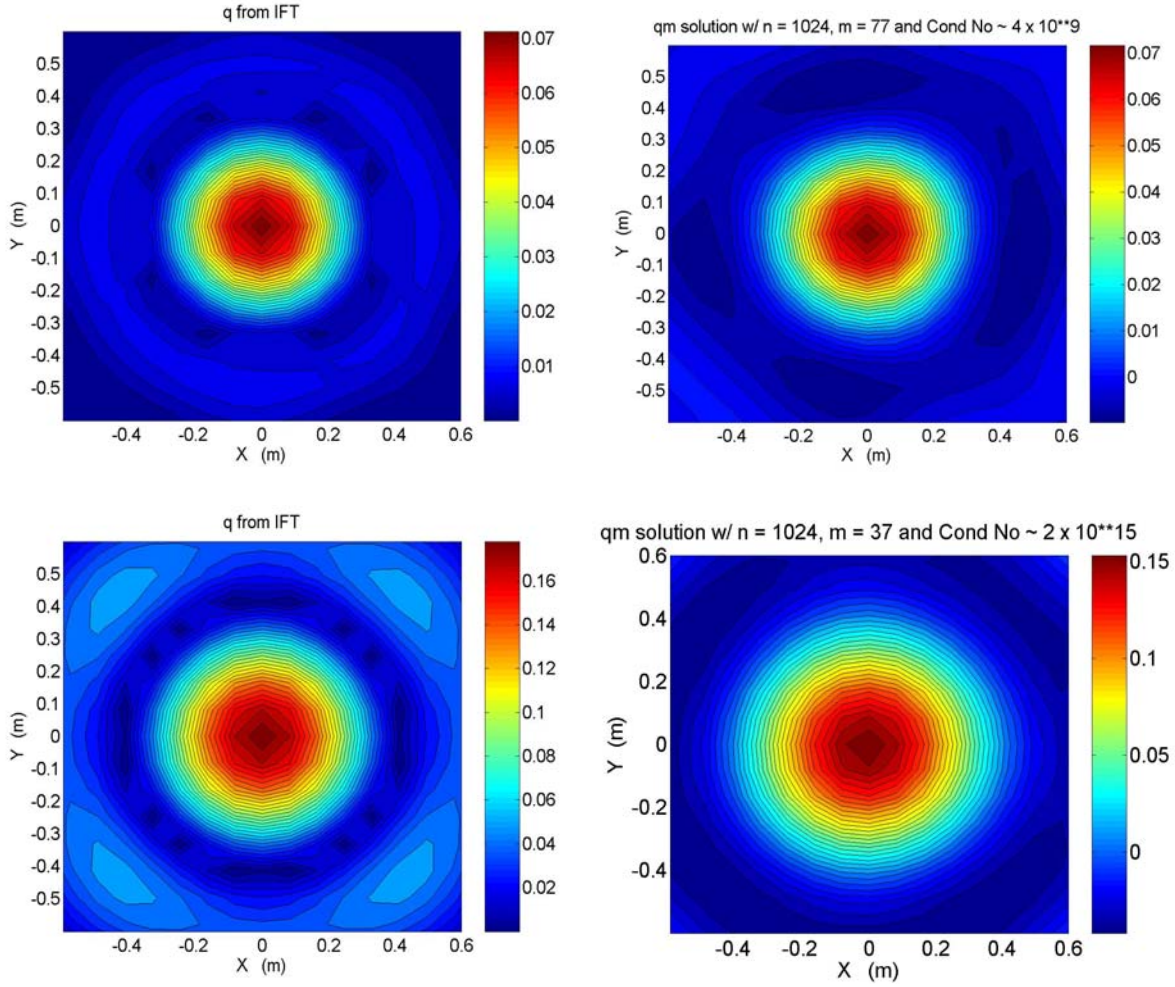
Figure 29. Source solutions for S_0 surfaces deeper than that (Zq = 0) in Figure 28. Here Zq = -0.25 (top) and -0.5 (bottom), the latter being the depth of the point physical source. Left: q from frequency truncation. Right: q_m from eigen-system truncation.

Table 1. Depth Zq of surface S_0 containing equivalent sources q; approximate spatial width of the truncated q solution; condition number C of the governing matrix before truncation.

Zq	approx q width	C
0	1 m	$\sim 10^4$
-0.25 m	0.5 m	$\sim 4 \times 10^9$
-0.5 m	0.6 m	$\sim 2 \times 10^{15}$

To distinguish better between the performances of the two truncation systems, we perform another test with somewhat more realistic i.e. complex patterns in the relevant quantities. While the target is again at Z = -0.5 m, its moment here is $\mathbf{m}$ = [0,1,1], as if it is tilted (the previous vertical dipole had $\mathbf{m}$ = [0,0,1]). Further, a non-vertical $\hat{\mathbf{B}}_e$ is assumed, in particular, that which applied at the APG test site, $\hat{\mathbf{B}}_e$ = [-0.08, 0.38, -0.92]. Computations for both truncation systems were performed with α = 0.01 and *RelNoiseMag* = 0.01. The changes introduced relative to the first test produce more complicated signal distributions and $V(\mathbf{k})$ patterns. Evidently the eigen-structure of the system is also more complicated in such a way that simple truncation has unanticipated and unwelcome effects. The computed q distributions in Figure 30 show that frequency truncation produced an orderly shape reflecting the Y-Z tilt of the target. The eigen-system truncation results are irregular and do not show the physical Y-Z spread of source action in the central cluster. Further (Figure 31), when the data on the measurement plane is reconstructed using these truncated q solutions, that from the frequency truncation approach is much superior in both magnitude and shape.

Whether this picture might be altered by some sort of strategic manipulation of particulars in the truncation systems - e.g. adjustment of α or other means of selecting residual participants in the eigen-solution - must be determined by subsequent research. Overall, as they stand these results suggest that eigen-system truncation could not be relied upon either for downward solution for source concentrations or for computation of above-ground signals. Frequency truncation appears able to produce tolerable equivalent source distributions, albeit limited in their concentration, with the ability to compute consistent above-ground signal patterns.
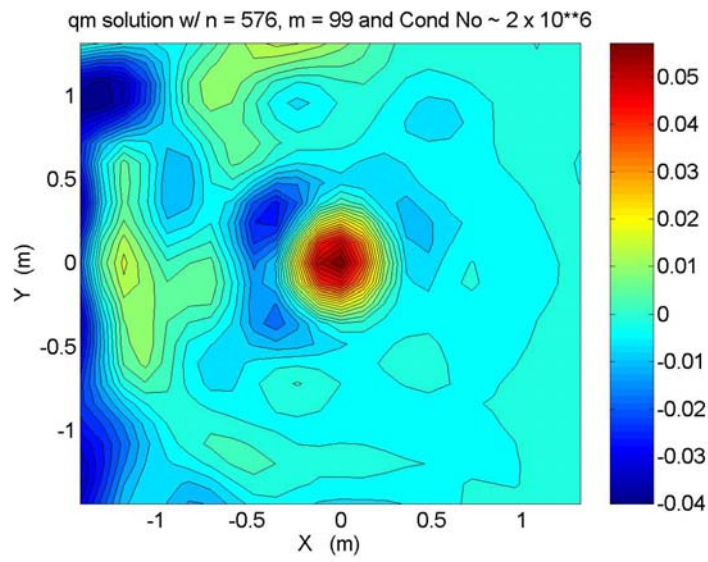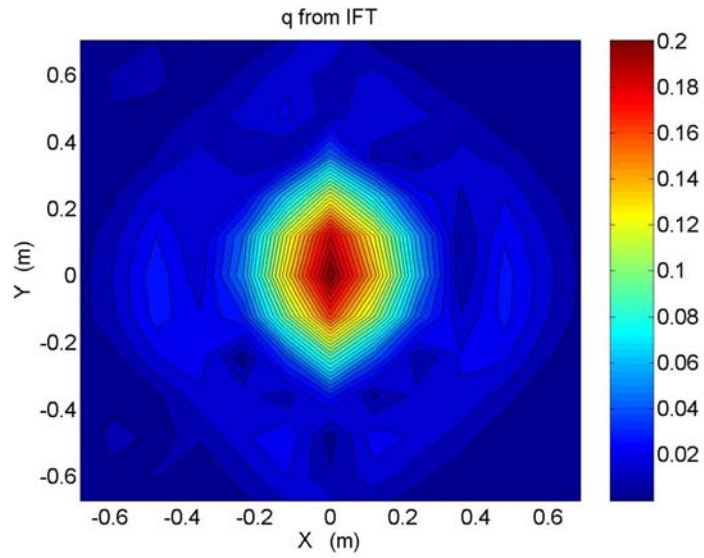
Figure 30. Truncated solutions for equivalent source distributions with Zq = -0.25 when the physical target is at -0.5 m. Top: frequency truncation. Bottom: Eigen-system truncation.
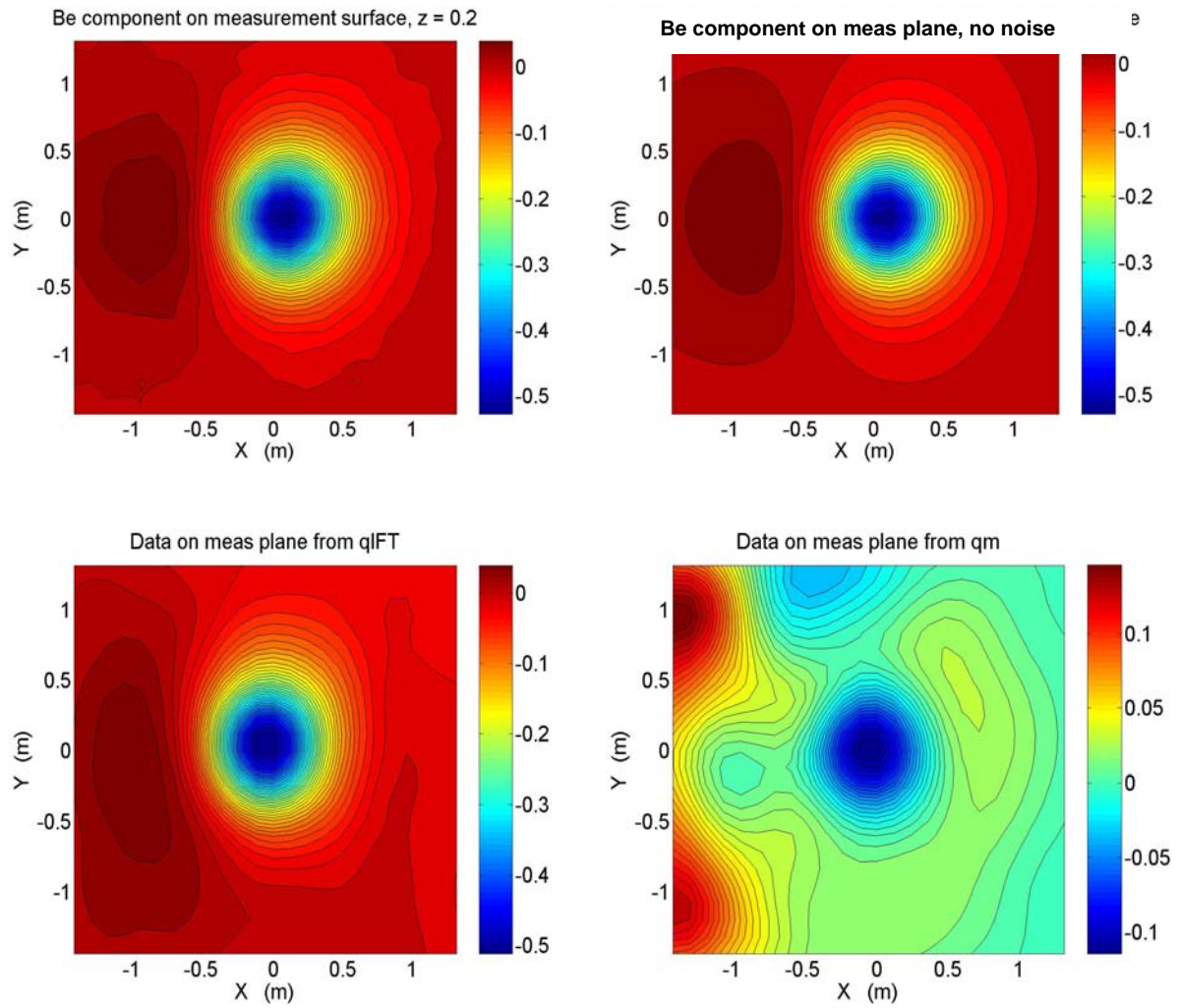
Figure 31. Distributions of the data on the measurement plane S_m. Top: "Actual" data with (left) and without noise (right). Bottom: Data on measurement plane reconstructed from truncation solutions based on the noisy data, derived from the frequency (left) and eigenvalue truncation solutions for q (right).

5.2.3. Control of Clutter Amplification as Well?

As a last experiment, consider a case again with the earth's field vertical, including a vertical dipole target ($\mathbf{m} = [0, 0, 1]$) at 60 cm depth, offset from which is a piece of clutter ($\mathbf{m} = [0, 0, 10^{-1}]$ at 20 cm depth. In order to focus on amplification of the clutter source at depth (see Section ***), we assume no random noise in the data such might be amplified by any ill-conditioning. As S_0 is lowered the computations produce the equivalent source distributions in Figure 32, both with ($\alpha = 0.01$) and without frequency truncation. For a source plane S_0 on the "ground surface" (Zq = 0) above both items, both direct (non-truncated) and truncated solutions are the same . At Zq equal to the clutter depth, the solutions are dominated appropriately by the clutter item, more so in the direct solution. With deeper S_0 the direct solution is increasingly dominated by the sources pertaining to the clutter, which spread and increase in magnitude. Additionally, with C increasing to $\sim 5 \times 10^{11}$ at Zq = 60 cm, any noise whatsoever in the data would have further swamped the direct solution, causing high amplitude, high frequency oscillations over the entire domain. However, in our noiseless example, the frequency-truncated solution retains a more appropriate character and magnitude, some distortion notwithstanding. Perhaps most notably, the frequency truncation appears to restrain the tendency of the clutter-related sources to dominate the solution at depths greater than the clutter item itself. This implies some limited deletion of signal content in the sense that a reconstruction of the data on the measurement plane S_m from the truncated q at Zq = 60 cm shows limited resolution (Figure 33). However, the gross features and appropriate magnitude of the data are retained.

Zq =0

Zq=20cm

Zq=40cm

Zq=60cm
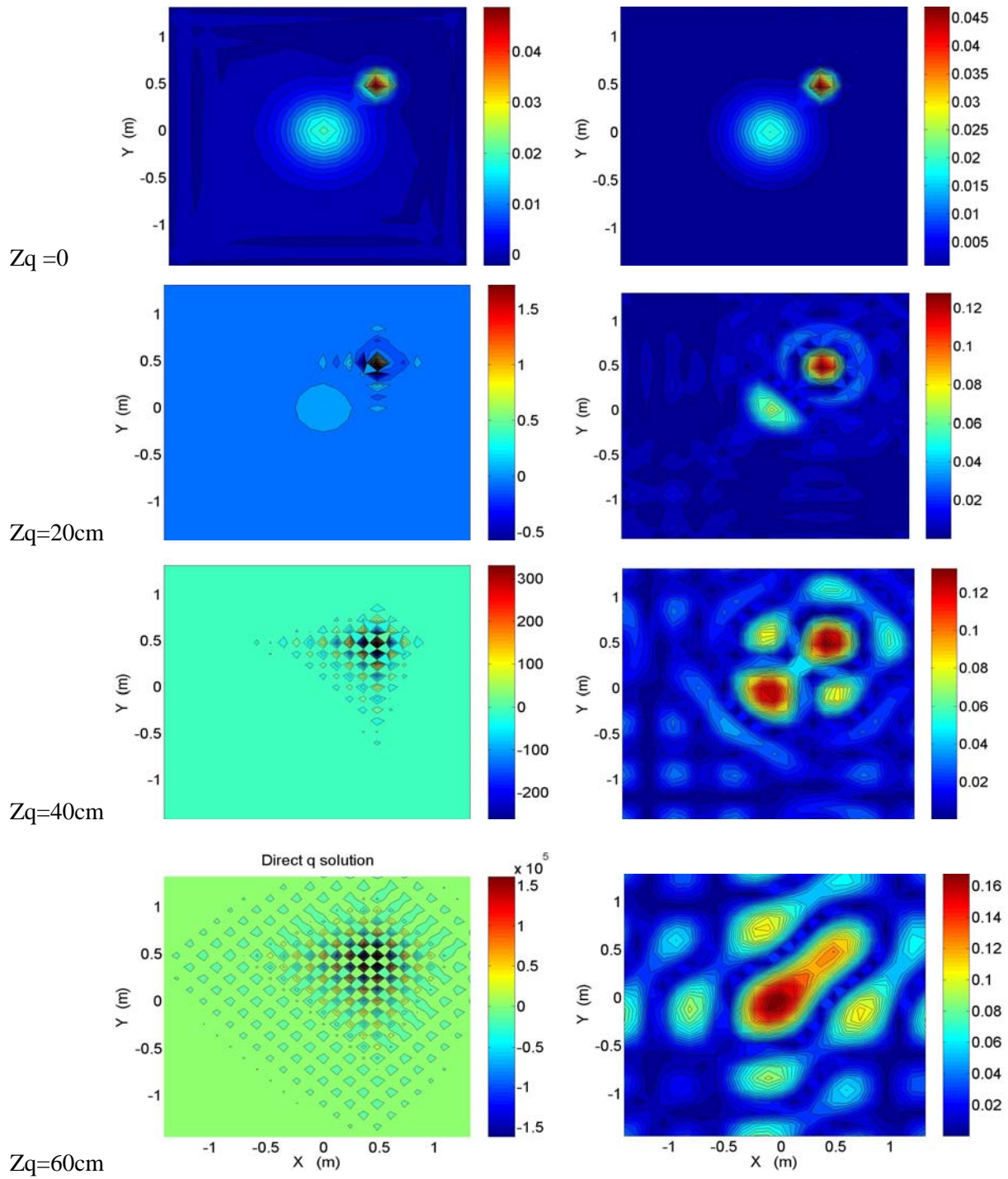
Figure 32. Equivalent source distributions computed on planes at various depths, Zq. Left: Direct solution (no truncation). Right: Frequency truncation.
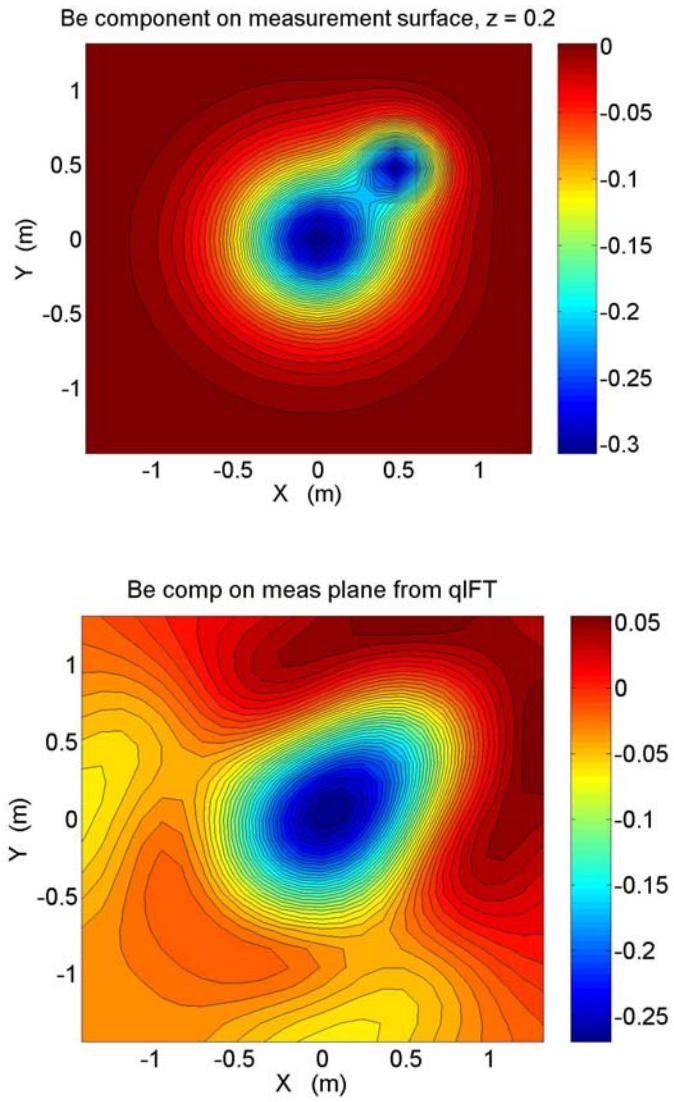
Figure 33.. Same case as above, showing reconstruction of the data on the measurement plane S_m from the truncated q at Zq = 60 cm.

6. References

1. S.D. Billings, J.M. Stanley, and C. Youmans (2002). Magnetic discrimination that will satisfy safety regulators, Countermine Forum 2002 (CD), Orlando, FL.

2. F.S. Grant and G.F. West (1965). Interpretation Theory in Applied Geophysics, McGraw-Hill, 583 pp.

3. W.M. Telford, L.P. Geldart, and R.E. Sheriff (1995). Applied Geophysics, 2nd edition, Cambridge Univ. Press., 770 pp.

4. J.M. Reynolds (1997). An Introduction to Applied and Environmental Geophysics, John Wiley & Sons, 796 pp.

5. J.D. Jackson (1998). Classical Electrodynamics, 3rd Edition, John Wiley & Sons, 808 pp.

6. D.K. Cheng (1983). Field and Wave Electromagnetics, Addison-Wesley, 576 pp.

7. K. O'Neill, K. Sun, F. Shubitidze, I. Shamatava, and K.D. Paulsen (2006). Accounting for the effects of widespread discrete clutter in subsurface EMI remote sensing and discrimination, IEEE Trans. Geosci. Remote Sens., Vol 44, No. 1, 32-46.

8. L. Helms and J.M. Stanley (2003). Sub-Audio Magnetics: Technology for Simultaneous Magnetic and Electromagnetic Detection of UXO, ESTCP Fact Sheet. See also annual/final reports as they emerge.

9. W.M. Wynn (1999). "Detection, Localization, and Characterization of Static Magnetic Dipole Sources," Chapter 11 in *Detection and identification of Visually Obscured Objects*, C.E. Baum (ed), Taylor & Francis.

10. D.R. Lynch (2005). *Numerical Partial Differential Equations for Environmental Scientists and Engineers: A First Practical Course*, Springer, 388 pp.

11. F. Shubitidze, K. O'Neill, S. Haider, K. Sun, and K.D. Paulsen (2002). Application of the method of auxiliary sources to the wideband electromagnetic induction problem, IEEE Trans. Geosci. Remote Sens., vol 40, No 4, 928-942, 2002.

12. F. Shubitidze, K. O'Neill, K. Sun, and K.D. Paulsen (2004). Investigation of broadband electromagnetic induction scattering by highly conductive, permeable, arbitrarily shaped 3-D objects, IEEE Trans. Geosci. Remote Sens., Vol 42, No. 3, pp 540-556.

13. F. Shubitidze, K O'Neill, K. Sun, I. Shamatava and K.D. Paulsen (2004). A hybrid full MAS and combined MAS/TSA algorithm for electromagnetic induction sensing, Appl. Comp. Electromagn. Soc. J., vol 19, no 1b, 112-126.